Challenging the turbidity current maximum run-up height paradigm

Ru Wang[1*], Mia Hughes[1], David M. Hodgson[1], Jeff Peakall[1], Helena C. Brown[1], Gareth M. Keevil[1] and Ed Keavney[1]

[1] *School of Earth & Environment, University of Leeds, Leeds, LS2 9JT, UK*

Correspondence: Ru Wang (earrwa@leeds.ac.uk)

This paper is a non-peer reviewed preprint submitted to EarthArXiv and will be submitted to *Geophysical Research Letters* or *Nature Communications*.

ABSTRACT

Turbidity currents are a primary mechanism for transporting sediments, pollutants, and organic carbon into the deep ocean. They are strongly influenced by seafloor topography because of their relative bulk density and associated gravitational influence being 3-4 orders of magnitude smaller than in terrestrial systems. Marked run-up of turbidity currents on slopes poses a hazard to seafloor infrastructure, and leads to distinctive depositional patterns, yet the prediction of run-up heights remains poorly understood because the present calculations are derived from 2D experimental configurations and/or numerical modelling and merely limited to scenarios in which the flow strikes the topographic barriers orthogonally.

Here we present the results of 3D experiments in unconfined settings that are used to develop a new analytical model that improves the prediction of maximum run-up heights of turbidity currents that encounter topographic slopes of varying gradients and flow incidence angles. We show that existing predictive models based on 2D confined flows focusing on frontal topographic configurations underestimate the run-up heights of turbidity currents by approximately 15-40%. Experimental results highlight the importance of considering the energy contribution from internal pressure in the fluid, cross-stream and/or vertical velocities and lateral flow expansion and divergence in unconfined flows. Our findings reveal that intermediate slope gradients (ca. 30°) and (near-)perpendicular flow incidence angles generate the highest run-up heights, up to 3.3 times the flow thickness. Novel analytical models are presented subsequently for predicting maximum run-up height as a function of both the gradient and incidence angle, comparing the models to the newly observed data. Such models provide relatively more realistic estimates of run-up heights for flows on three-dimensional slopes typical of natural systems.

These findings are critical for improving sediment transport models, predicting the distribution of sediments, pollutants, and organic carbon in deep-sea environments, assessing seafloor geohazards, and reconstructing ancient deep-water basin palaeogeographies.

INTRODUCTION

Turbidity currents are subaqueous, gravity-driven turbulent flows and are the primary mechanism for transporting clastic sediments, microplastics, organic carbon, and dissolved nutrients and pollutants from continental shelves to the deep ocean (e.g., Kuenen and Migliorini, 1950; Dzulynski et al., 1959; Sestini, 1970; Normark et al., 1993; Kneller and Buckee, 2000). These flows also present a significant geohazard and can cause catastrophic damage to seafloor infrastructure, such as pipelines and communication cables (Carter et al., 2014). Turbidity currents, along with other sediment gravity flows, commonly traverse seafloor terrain characterized by substantial topography (e.g., Normark, 1985; Apps et al., 1994; Kneller and McCaffrey, 1999), which is typically generated related to mass transport deposits, volcanic features, tectonic deformation, salt or mud diapirism, and even abyssal plain mountains. Such topography exerts a strong influence on the behaviour of turbidity currents, notably altering their velocity and sediment concentration profiles, which in turn affects their sediment transport capacity (e.g., Kneller et al., 1991; Edwards et al., 1994; Patacci et al., 2015; Tinterri et al., 2016, 2022; Dorrell et al., 2018; Soutter et al., 2021; Keavney et al., 2024; Reece et al., 2024a,b). Where the relief of the seafloor is sufficiently elevated, the turbidity current may be blocked entirely. However, due to their reduced excess density—2–3 orders of magnitude smaller than rivers in terrestrial systems—turbidity currents, especially the dilute upper portion of the fluid, can ascend topographic barriers several times their flow thickness via a process known as superelevation (e.g., Rottman et al., 1985; Muck and Underwood, 1990; Lane-Serff et al., 1995; Kneller and McCaffrey, 1999; Keavney et al., 2024). In submarine canyon systems, the Coriolis and centrifugal forces may further enhance the vertical run-up by generating lateral pressure gradient forces in a canyon bend (e.g., Komar, 1969; Pirmez and Imran, 2003; Straub et al., 2008; Lamb et al., 2008).

The phenomenon of turbidity current run-up on topographic slopes and the resultant deposition of turbidites at elevations higher than the initial flow base has been documented in laboratory experiments (e.g., Muck and Underwood, 1990; Soutter et al., 2021; Keavney et al., 2024), modern and ancient field studies (e.g., Damuth and Embley, 1979; Cita et al., 1984; Dolan et al., 1989; Wynn et al., 2010; Al A'Jaidi et al. 2004; Soutter et al., 2019). For example, turbidites collected from the Ceara Rise, western equatorial Atlantic, indicate a run-up flow on slopes of a horizontal distance of 40 km and a vertical distance of 150 ~ 400 m (Damuth and Embley, 1979). Ocean drilling core samples on the Tiburon Rise near the Barbados subduction zone demonstrate a transport distance of ca. 1000 km of the terrigenous turbidite sands from South America and a speculative vertical transfer of minimum 1,000 m (Dolan et al., 1989). The ability of turbidity currents to run up slopes and deposit materials at higher elevations exacerbates their threat as a geohazard to deep-sea infrastructure (e.g., Bruschi et al., 2006; Carter et al., 2014) and presents challenges for modern human-made water reservoir de-risking management (e.g., Wei et al., 2013). A comprehensive understanding of the factors governing these processes is crucial for predicting the distribution of plastic and other pollutants on seafloor topographic slopes (e.g., Haward et al., 2018; Kane et al., 2020), assessing the impacts on deep-sea oxygenation, and reconstructing the paleogeography of ancient deep-water basin-fills (e.g., Sinclair, 1994; Lomas and Joseph, 2004; Bell et al., 2018).

Despite their global importance, development of the theory on run-up elevation has mainly relied on numerical and physical modelling, possibly due to a lack of direct measurements of the interaction of unconfined turbidity currents and seafloor topography in the field. The existing models to predict maximum run-up elevation are primarily either based on scaleddown 2D narrow flume experiments and/or numerical modelling (Rottman et al., 1985; Muck and Underwood, 1990; Lane-Serff et al., 1995; Kneller and McCaffrey, 1999) and have been limited to scenarios in which the flow strikes the topographic barriers orthogonally. 2D flume-tank experiments suggest that the body of density currents striking a frontal topography may rise up the topography to a height 1.5 to 2.5 times the flow thickness (Rottman et al., 1985). Muck and Underwood (1990) noted the maximum run-up height of a subcritical turbidity current is approximately 1.53 times the flow thickness, based on a simple numerical analysis assuming a full conversion of kinetic energy to potential energy and frictional heat loss, with further validation from 2D laboratory experiments using saline density currents. However, the applicability of this predictive model into the natural world is questioned as it assumes a uniform flow density (i.e., neglecting lateral and vertical density gradients) and flow velocity. To date, Kneller and McCaffrey's (1999) analytical model represents the most common method for estimating the maximum run-up height of overflows of turbidity currents on obstacles, taking into consideration not only the energy balance from the kinetic energy (KE) of a current to the potential energy gained as it moves up a topographic slope (Chow, 1959; Hungr et al., 1984; Kirkgoz, 1983), but also the impact of flow density stratification and vertical flow velocity variations over height, typical of natural systems in the field. This model assumes that between the time of first encountering the topography and reaching its maximal elevation, a fluid parcel in the current at initial height z within the flow transfers all its kinetic energy into gravitational potential energy along with some energy lost to friction (cf. Allen, 1985; Muck and Underwood, 1990). Hence, the maximum run-up elevation h_{max} of any parcel of the density current is the sum of its initial elevation and its height gain, and is given by $h_{max} = z + \frac{\rho_z {u_z}^2(1-E)}{2g\Delta\rho_z}$, where u_z is the component of velocity at initial height z that is normal to the topography, g is gravitational acceleration, ρ_z is the density of the fluid at initial height z, $\Delta\rho_z$ is the density difference between ρ_z and the ambient fluid and E is the frictional energy loss relative to the initial KE. The predicted maximum run-up height H_{max} of the overall flow is then the maximum value of this estimated h_{max} for all the fluid parcels.

However, the applicability of these existing models, especially the Kneller and McCaffrey (1999) method, into 3D, unconfined settings is yet untested. The present paradigms do not account for the effect of different configurations of topographic slopes, i.e., incidence angle of the flow onto the slope and slope gradient (**Fig. 1**). Furthermore, the lateral variability in maximum run-up height potential on slopes in a strike direction, its characteristics as a function of slope orientations and slope angles and therefore their potential impact on the magnitude of maximum upslope run-up height is rarely explored (**Fig. 1**).

Here we develop a generic framework to predict the maximum run-up height up slopes when 3D, unconfined turbidity currents encounter topographic slopes with different configurations, including incidence angle of the flow and slope gradient. First, we present the first experimental measurements of run-up height notably in unconfined settings under controlled laboratory conditions, using sustained, saline density currents, where the flow interacts with a planar topographic slope of varying gradients, at a range of flow incidence angles. The flows were designed to be unable to overtop the topographic slope but could flow downstream around the slope. We utilised dissolved salt to represent fine mud in suspension that does not easily settle out, and moves in bypass mode, and therefore flows herein can be considered to model low-density turbidity currents (Sequeiros et al., 2010; Keavney et al., 2024; Reece et al., 2024a, b). Second, we present a novel analytical model to predict maximum run-up height as a function of both the slope gradient and incidence angle, comparing the models to the newly observed experimental data. These newly developed numerical models afford relatively more realistic estimates of run-up heights for unconfined flows on 3D slopes.

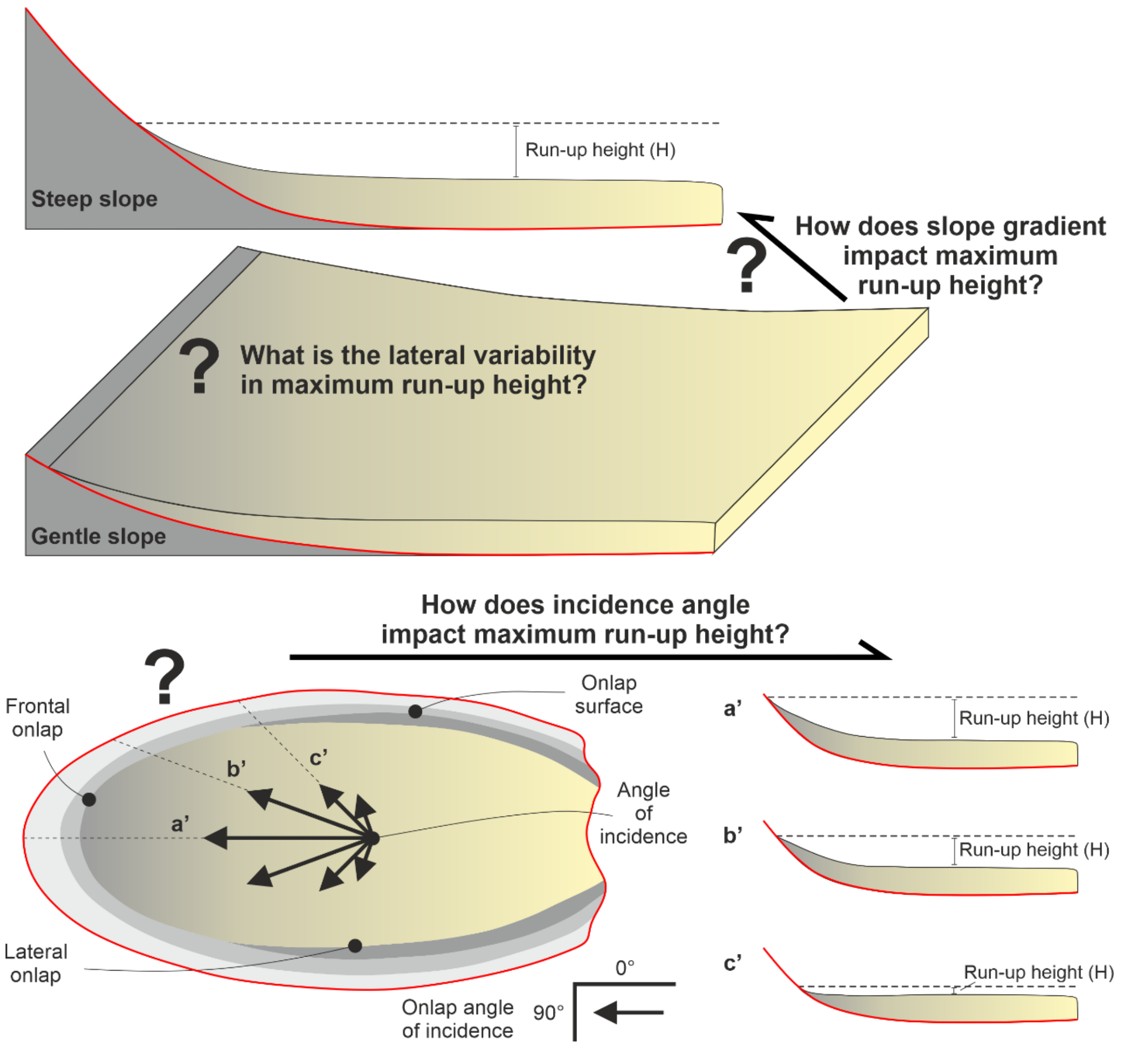

Fig. 1. Schematic diagram illustrating the existing knowledge gaps in the understanding of the characteristics of run-up height potential of turbidity currents interacting with topographic slopes.

RESULTS

General flow behaviour of the ramp experiments

A summary of the general flow behaviour in the ramp experiments and a representative video of Experiment S40°IN75° is given in the **Supporting Information** (**Video S1**), with details documented in Keavney et al. (2024) and Wang et al. (2024). Notably, when the flow exits the channel, it moves as an unconfined density flow along the basin floor (**Fig. 2**). Once the flow encounters the ramp, it decelerates and strikes the topographic slope with a strong flow divergence character on the slope surface. Subsequently, the flow stratifies into a denser lower part and a more dilute upper part. The dilute, upper part can run up the slope, thinning until it reaches its maximum height H_{max} ('maximum run-up height', hereafter; cf. Pantin and Leeder, 1987; Edwards et al., 1994). The lower part collapses back down, either deflecting parallel to the slope or reflecting towards the inlet. The flow stripping zone on the slope can be quantified by the height of the initial reversal of the dense lower flow H_{min} and the maximum run-up height H_{max}(Keavney et al., 2024). The initial reversal of the flow can undercut the outbound flow and migrate upstream, leading to a thickening of the entire body of the density current, known as an unsteady flow inflation phase. Eventually, as the parental flow re-establishes, the thickening body of the density current in the basin becomes flat-topped, a quasi-stable flow front develops on the slope surface. Finally, as the inlet flow wanes, the entire body of the turbidity current collapses.

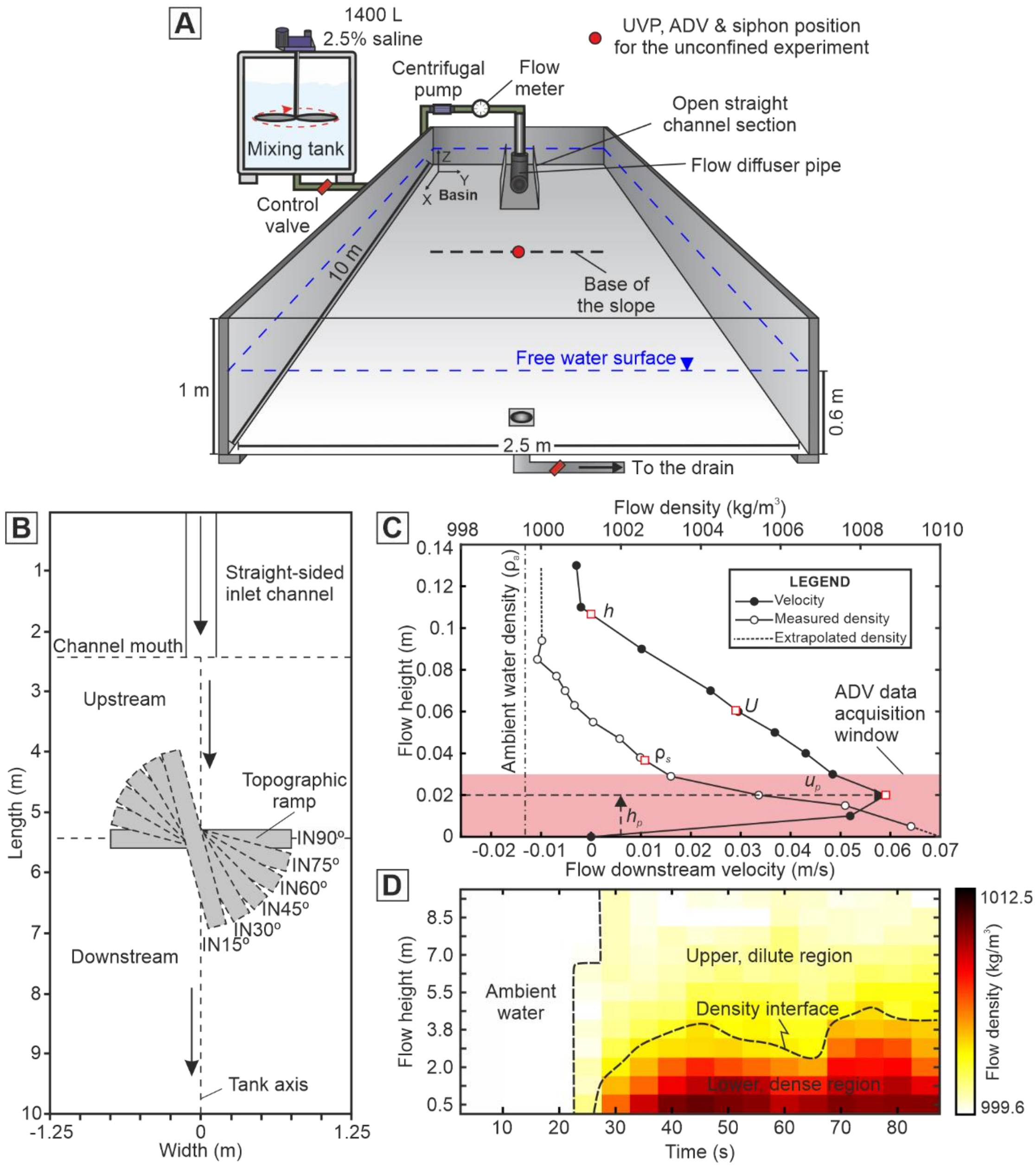

Fig. 2. (A) Schematic sketch of the experimental facility. The base of the topographic ramp is shown as a black dashed line. The positions of the Ultrasonic Velocity Profiler (UVP), Acoustic Doppler Velocimeter (ADV) and siphoning system for the unconfined experiment is also indicated. (B) Topographic configurations for ramps with different incidence angles relative to the incoming flow shown in a plan view. (C) Profiles of time-averaged flow downstream velocity and density for the experimental density current recorded at 3 m downstream from the channel mouth along the channel-basin centreline in the unconfined reference experiment. Both measurements were initiated 5 s after the current head passed and lasted for 30 s. The flow

depth h, maximum downstream velocity u_p, its height above the basin floor h_p, depth-averaged downstream velocity U and depth-averaged density ρ_s are shown as red squares. The ambient water density ρ_a was measured at 12 °C. (D) Time-series profiles of flow density measured at 3 m downstream of the channel mouth along the channel-basin centreline. Modified after Keavney et al. (2024).

Maximum run-up distance and height on slopes in the ramp experiments

Global distribution and comparison with existing models

The measured maximum run-up distance L_{max} and height H_{max} for all the ramp experiments ranges from approximately 2.3 to 7.9 times flow thickness and 1.3 to 3.3 times flow thickness, respectively (**Fig. 3**). The measured maximum run-up height in our frontal experiments (Experiments S20°IN90°, S30°IN90° and S40°IN90°) is shown to be approximately 2.5 ~ 2.7 times flow thickness, which is relatively higher than those predicted by the Kneller and McCaffrey (1990) (see **Supporting Information 2** for the details on the modelled estimation) and the Muck and Underwood (1990) methods and marginally higher than the upper limit of the prediction interval by Rottman et al. (1985).

Variation of incidence angles of the current onto the slope

Maximum run-up distance and height on slopes as a function of incidence angles of the current with the slope are examined for experiments with the same slope gradient (**Fig. 3G, 3I**). Notably, for lower incidence angles, the maximum run-up distance on slopes decreases markedly (L_{max} = 0.44 m to 0.87 m for experiments of slope gradient of 20°; L_{max} = 0.28 m to 0.72 m for experiments of slope gradient of 30°; L_{max} = 0.25 m to 0.45 m for experiments of slope gradient of 40°; **Fig. 3G**). However, in Experiment S30°IN90°, the maximum run-up distance on slopes reaches ca. 0.55 m, which is unexpectedly shorter than that documented in experiments S30°IN75°, S30°IN60° and S30°IN45° (L_{max} = 0.72, 0.59 and 0.58 m,

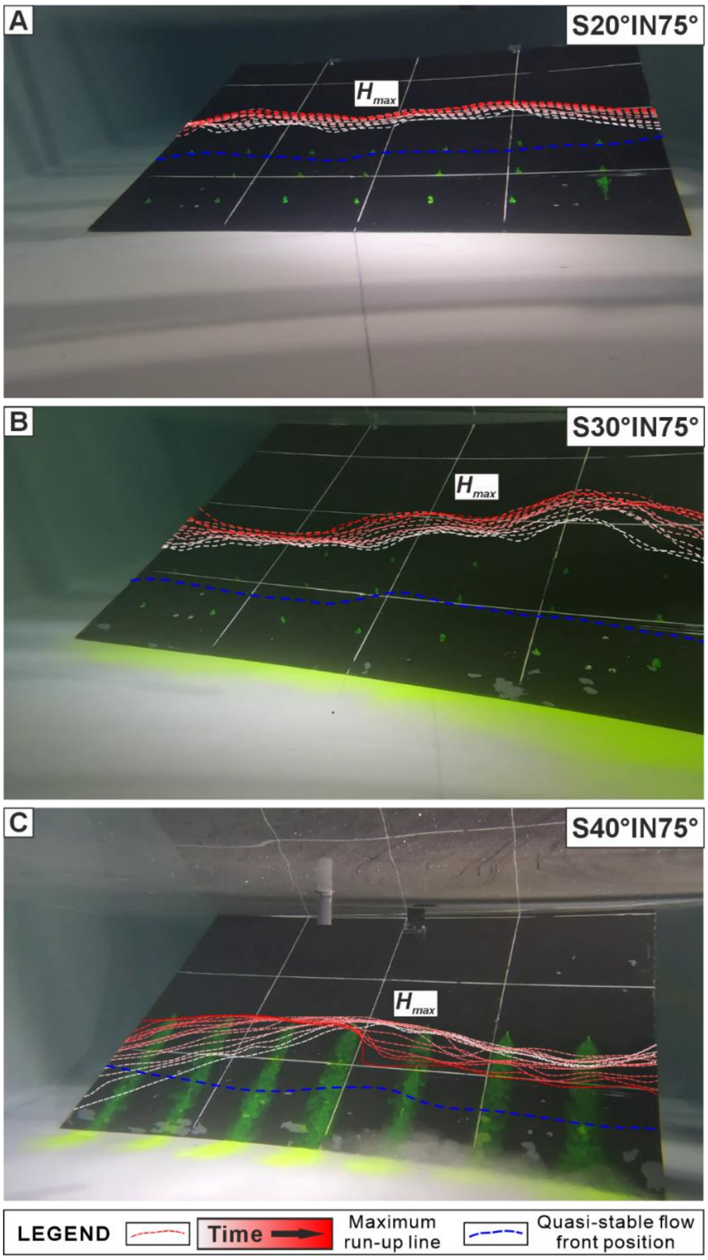

Fig. 3a. Representative front-view photographs depicting the fluctuations of maximum run-up line on the topographic slope for experiments with different slope angles of topographic slope (Experiments S20°IN75°, S30°IN75°and S40°IN75°). H_{max} denotes the maximum height that the dilute, upper part of the flow can run up on the slope surface. Red dashed line indicates the

maximum run-up line, colour-coded according to time. Here, a 15 s time window (1 s time interval) after the achievement of the maximum run-up point is chosen to demonstrate the fluctuations of the maximum run-up line. Blue dashed line represents the location of quasi-stable flow front.

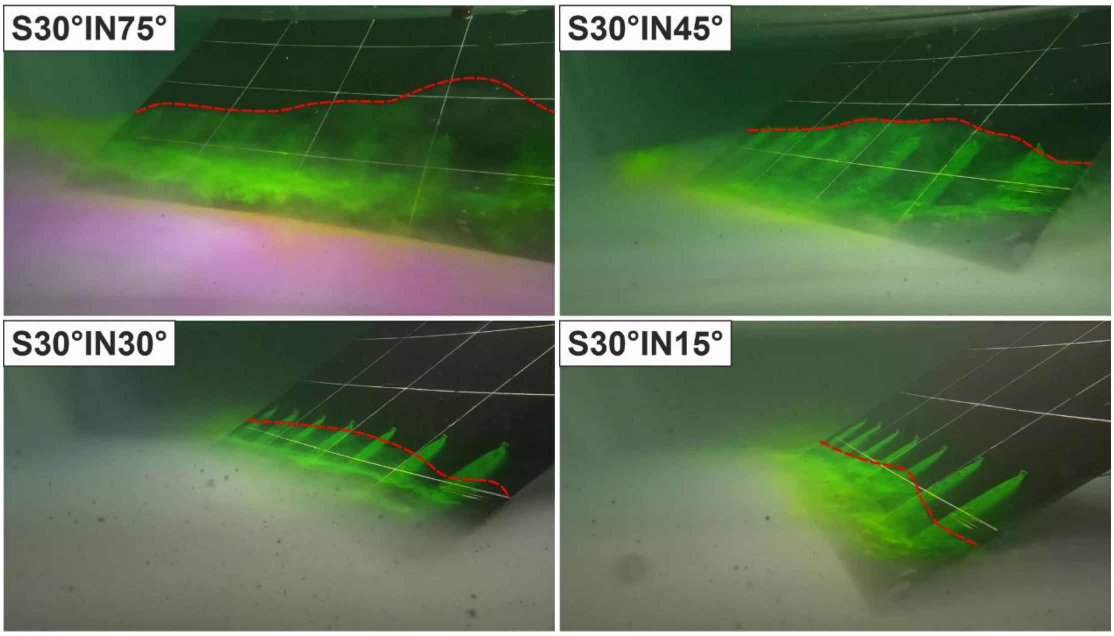

Fig. 3b. Representative front-view photographs depicting the geometry of the maximum run-up line on the topographic slope for experiments with different incidence angles of the current onto the slope (Experiments S30°IN75°, S30°IN45°, S30°IN30° and S30°IN15°). H_{max} denotes the maximum height that the dilute, upper part of the flow can run up on the slope surface.

respectively). A similar positive relationship is identified between maximum run-up height on slopes versus incidence angles of the current onto the slope (H_{max} = 0.15 ~ 0.30 m, ca. 1.4 to 2.7 times the flow thickness for experiments of slope gradient of 20°; H_{max} = 0.14 ~ 0.36 m, ca. 1.3 to 3.3 times the flow thickness for experiments of slope gradient of 30°; H_{max} = 0.16 ~ 0.30 m, ca. 1.5 to 2.7 times the flow thickness for experiments of slope gradient of 40°; **Fig. 3I**). However, in Experiment S30°IN90°, the maximum run-up height on slopes reaches ca. 0.28 m (ca. 2.5 times flow thickness), which is lower than that observed in experiments

S30°IN75°, S30°IN60° and S30°IN45° (H_{max} = 0.36, 0.29, and 0.29 m, respectively, ca. 3.3, 2.6 and 2.6 times flow thickness).

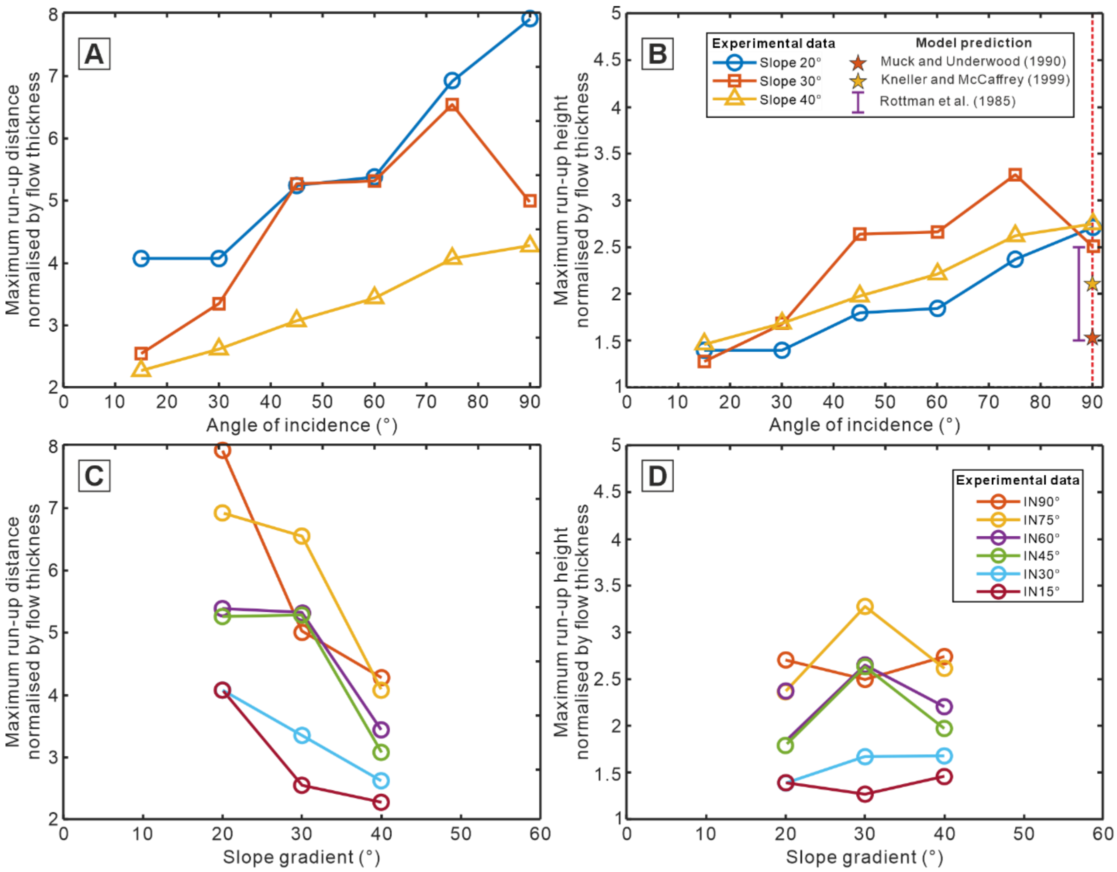

Fig. 3c. (A-B) Plots of non-dimensional maximum run-up distance and height of the density currents on the barrier ramp versus the incidence angle of the current onto the slope. (C-D) Plots of non-dimensional maximum run-up distance and height on the barrier ramp versus the angle of the topographic slopes. In panel B, the predictive values and/or interval of maximum run-up elevation in frontal experimental setting (i.e., the flow incidence angle onto the slope is 90°) based on previous models are indicated. The yellow and red stars represent the values predicted by Kneller and McCaffrey (1999) and Muck and Underwood (1990) methods, respectively. The purple range symbol is the 1.5 to 2.5 range, predicted by the model of Rottman et al. (1985).

Variation of slope gradients

Maximum run-up distance and height on slopes as a function of the slope angles of the topographic slopes are examined for experiments with a single incidence angle of the current onto the slope (**Fig. 3H, 3J**). An inverse relationship is seen between maximum run-up distance on slopes versus slope gradient, i.e., a gentler topographic slope corresponds to a longer maximum run-up distance on slopes (e.g., L_{max} = 0.44 ~ 0.87 m for experiments of incidence angle of 90°; L_{max} = 0.38 ~ 0.59 m for experiments of incidence angle of 60°; L_{max} = 0.25 ~ 0.45 m for experiments of incidence angle of 15°; **Fig. 3H**). The relationship between maximum run-up height versus the gradient angle of the topographic slope is more complicated (**Fig. 3J)**. In an oblique experimental configuration with the same incidence angle of the flow to the slope, the maximum run-up height for a slope of 30˚ is higher than that for a 20˚ slope, which paradoxically occurs higher than a 40˚ slope. In a highly oblique and frontal experimental configuration (e.g., Experiments IN15° and IN90°), only a slight difference is documented in maximum run-up height across experiments with different slope gradients (e.g., H_{max} = 0.15 m, 0.14 m and 0.16 m, respectively in Experiment S20°IN15°, Experiment S30°IN15° and Experiment S40°IN15°, ca. 1.3 ~ 1.5 times flow thickness). In a frontal configuration, the maximum run-up height for a slope of 30˚ is marginally lower than that of a slope of 20˚ and 40˚ (H_{max} = 0.28 m, ca. 2.5 times flow thickness in Experiment S30°IN90° versus H_{max}= 0.30 m in Experiment S20°IN90° and Experiment S40°IN90°, ca. 2.7 times flow thickness).

Revisiting the existing paradigm of maximum run-up height estimation

The large superelevation of the density currents observed in our laboratory experiments compared to the existing predictive models on the maximum run-up height of sediment gravity flow interaction with slopes (Rottman et al., 1985; Muck and Underwood, 1990; Lane-Serff et al., 1995; Kneller and McCaffrey, 1999) challenge the validity of these commonly used methods, especially Kneller and McCaffrey's (1999) method, into the 3D unconfined settings. This might be ascribed to the fact that (i) the fluid parcel that reaches H_{max} is pushed forward by the flow behind it (and the pressure gradient due to the density gradient between the saline and ambient water); (ii) in an unconfined turbidity current setting, not only the downstream velocity, but also the vertical and/or cross-stream velocity components contribute to the initial kinetic energy, which therefore tends to transfer into higher potential energy and consequently comparatively higher upslope run-up height.

Crucially, our experimental observations show that the maximum run-up height of turbidity currents on slopes is a function of both slope gradient and flow incidence angle onto the topographic slopes (**Fig. 3I and 3J**), which were not incorporated in the existing predictive models. A noticeable decrease in maximum run-up height on slopes with a lower flow incidence angle onto the slope (**Fig. 3I**) is mainly due to a decreased degree in topographic containment, and reduced velocity component normal to the topography which could contribute to run-up. However, our experiments herein also show an anonymously lower value in H_{max} for Experiment S30°IN90° compared to its counterparts with incidence angles of 75° and 60°. This might be attributed to the diverse dominant flow behaviour across experiments with different slope gradients (further discussion on this is presented later). Based on experimental work on unconfined turbidity currents interacting with orthogonal topography, Keavney et al. (2024) highlighted that the dominant flow processes transition from laterally divergence-dominated, through reflection-dominated, to deflection-dominated as the slope gradient changes from 20° to 40°. Here, as the flow process is dominated by flow reflection at the base of the slope in Experiment S30°IN90°, we interpret that much less the initial kinetic energy is contributed to transfer into potential energy, leading to the anonymously low value in H_{max} (**Fig. 3I**).

Without energy dissipation, the maximum run-up height would be independent of slope angle (Allen, 1985; Pantin and Leeder, 1987; Simpson, 1987). Taking frictional heat loss and turbulent dissipation into consideration, reducing the slope angle of the topography should lead to a lower maximum run-up height because at a lower slope gradient a larger horizontal flow distance is required to reach a given elevation (**Fig. 3H**), and in travelling this greater distance more energy is dissipated. The lack of dependence of maximum run-up height from slope angle in our frontal experiments (**Fig. 3J**) might be ascribed to a relatively short flow travel distance on the slope and therefore a negligible variation in the effects of energy dissipation on the ultimate run-up elevation. However, in the experimental results herein we found that in oblique experimental configurations, H_{max} exhibited a significant dependence on slope gradient; when the incidence angle of the current onto the slope is kept uniform and lying in the range from 30˚ to 85˚, H_{max} for a 20˚ slope was consistently lower than that for a 40˚ slope, which in turn was surprisingly lower than that for a 30˚ slope (**Fig. 3I**).

Another big difference between our experimental observations and the modelled prediction is that pronounced lateral flow expansion (i.e., transverse to the flow direction) and flow divergence phenomenon occurs in our 3D unconfined experiments (**Video S1**; Keavney et al., 2024 and Wang et al., 2024). This lateral and diverging flow component is overlooked in previous predictive models. It is hypothesised that the strength of the lateral flow expansion and the resultant different levels of rugosities of the geometry of the maximum run-up line on the slope surface along strike direction (**Supporting Information 3; Fig. 3**) would affect the ultimate maximum run-up height. In oblique experimental configurations, the observed greater value of H_{max} for a 30˚ slope compared to those for a 20˚ and 40˚ slope might be attributed to the lower amount of lateral flow expansion for a 30˚ slope (Keavney et al., 2024 and Wang et al., 2024) and a resultant higher rugosity in the geometry of the lateral maximum run-up line on the slope surface along the strike direction, compared to its counterparts for a 20˚ and 40˚

slope (**Supporting Information 3; Fig. 3**). A high rugosity in maximum run-up line geometry on the slope surface tends to contribute to a higher H_{max} value than modelled predictions, on the basis of 2D confined turbidity current settings. It appears that a fluid parcel H_{max} must receive additional energy from the force of the flow behind it, and from the pressure gradient at the boundary between the saline and ambient water, allowing it to reach a greater elevation than the Kneller and McCaffrey (1999) approach predicts.

The above-mentioned information adds complexity to the existing paradigms and highlights the need for updated predictive models that can capture these multidimensional interactions in 3D environments.

Numerical modelling

Our experimental data on observed maximum run-up height (**Fig. 3I**) challenges the application of existing methods for estimating upslope run-up elevation when turbidity currents encounter a frontal topographic slope in an unconfined setting. In this section, to address this issue, we introduce a novel numerical model that incorporates the effects of slope gradient angle (θ) and flow incidence angle (φ). The model is a further development of the Kneller and McCaffrey (1999) approach based on energy balance principles, accounting for kinetic energy, potential energy, work done by pressure, as well as frictional and turbulent dissipation (Allen, 1985; see **Supporting Information 4** for the details on the derivation of the predictive model). Like the Kneller-McCaffrey method, this model considers a fluid parcel at initial height z upon reaching the slope, approximating the parcel as retaining its density and structure throughout its journey up the ramp, effectively modelling it as a classical point particle. These broad approximations circumvent the need to solve any nonlinear hydrodynamic equations.

For simplicity, we assume an initial velocity $\vec{U} = (u, 0,\ 0)$ for each parcel of fluid meeting the ramp, with the x, y and z axes aligned with the downstream, cross-stream and vertical directions, respectively (**Fig. 2A**). The flow velocity u_z is averaged over all horizontal locations, with the subscript denoting its remaining dependence on vertical position z. The predicted run-up height for a fluid parcel at initial height (see **Supporting Information 4** for the details on the derivation of the predictive model) is

$$h_{max}(z) = z + \frac{\frac{1}{2}\rho_z {u_z}^2 \sin^2\varphi\,(\cos^2\theta + S\sin^2\theta) + \Delta\mathrm{E_{gain}}}{\Delta\rho_z\, g + \frac{F_{ave}}{\sin\alpha}} \quad (1)$$

with, again, the z subscripts referring to the density and velocity at height z. In the above equation, ΔE_{gain} is the energy gained from internal pressure and interactions of the fluid parcel with neighbouring fluid parcels; S is a dimensionless collision factor ranging from 0 to 1, characterising the fraction of kinetic energy associated with the normal component of the initial velocity that contributes to H_{max}; F_{ave} is the average dissipative force per unit volume, acting in the direction opposed to the fluid parcel's velocity; and the angle $\alpha = \tan^{-1}(\sin\varphi\tan\theta)$ represents the 'effective slope' of the ramp in the downstream (x) direction in the vertical (x, z) plane (**Fig. 4D**).

The overall H_{max} is the maximum h_{max} for all fluid parcels, and thus occurs when

$$\frac{d}{dz}\left(z + \frac{\frac{1}{2}\rho_z {u_z}^2 \sin^2\varphi\,(\cos^2\theta + S\sin^2\theta) + \Delta\mathrm{E_{gain}}}{\Delta\rho_z\, g + \frac{F_{ave}}{\sin\alpha}}\right) = 0 \quad (2)$$

To facilitate comparison to natural turbidity currents in the field, we normalise $h_{max}(z)$ by the flow thickness of the current body h and therefore Equation 1 changes into:

$$h_{max}(z)/h = z/h + \frac{\frac{1}{2}\rho_z {u_z}^2 \sin^2\varphi\,(\cos^2\theta + S\sin^2\theta) + \Delta\mathrm{E_{gain}}}{\left(\Delta\rho_z\, g + \frac{F_{ave}}{\sin\alpha}\right) h} \quad (3)$$

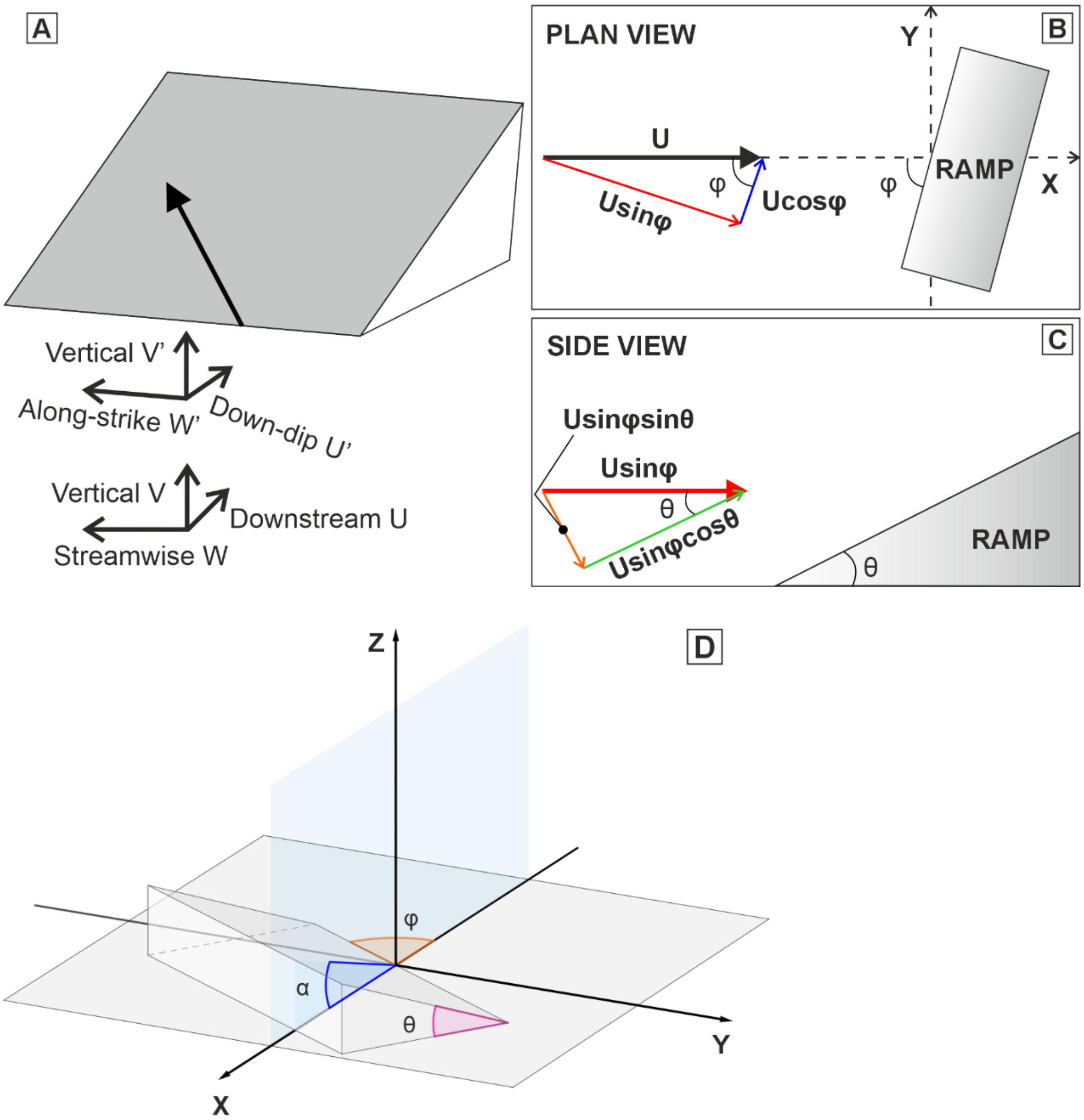

Fig. 4. Model conceptualisation of the numerical modelling work. (A) Model conceptualisation, showing an unconfined turbidity current interacts with topographic slope with a specific slope gradient and flow incidence angle. (B-C) Definition sketch illustrating the trigonometric relationships between the decomposed components of the initial velocity U in plan-view (B) and side view (C). (D) Schematic diagram demonstrating the 'effective slope' (α) between the flow path and the horizontal (x, z) plane, which is dependent on the flow incidence angle against the ramp and slope gradient. Here, $\sin\alpha = \sin(\tan^{-1}(sin\,\varphi\, tan\,\theta))$.

Note that the collision factor S, average dissipative force F_{ave} and energy gain from the surrounding fluid ΔE_{gain} are at this stage unknown variables, each requiring their own estimation, and are likely themselves to depend on the initial velocity, density and the angles φ and θ. However, in the present paper they will be approximated at zeroth order and treated as constant parameters. Finding more realistic estimates of these three unknown variables and their dependences on the initial parameters will be the subject of future research. In a relaxed way, F_{ave} can be approximated as $F_{ave} = \mu N$, where μ is the frictional coefficient and N is the normal contact force from the ramp, which should be equal to the component of the weight normal to the ramp: $N = \rho g' \cos\theta$. S is a dimensionless collision factor and determined by the properties of the inlet flow and the material of the slope surface.

Comparison of the numerical-model predictions with the observed experimental data

To test the validity of the numerical model above, its general run-up height predictions are compared to the observed values for each of the 18 ramp experiments herein, with the aim of approximating the overall dependence of (normalised) maximum run-up height on flow incidence angle and slope gradient. Due to the broad approximations made in the model and the turbulent nature of the flow ($Re \approx 3000$), only an approximate fit to the data is to be expected. To be fully realistic would require a Computational Fluid Dynamics simulation, but the purpose here is to provide a method of estimation that can be calculated quickly for practical purposes. Values of the input quantities representative of those measured in the current physical experiments in the first 5 s after the current head were substituted into the model (z = 0.045 m, ρ_z = 999.8 kg/m^3, $\Delta\rho_z$ = 0.22 kg/m^3, h = 0.11 m, u_z= 0.0243 m/s) as it is the dilute head of the density current that appears to mainly contribute to the maximum value of the run-up elevation over the course of the experiment (**Video S1**; **Fig. S2**). However, accurate values for the energy gain ΔE_{gain}, averaged dissipative force F_{ave} and collision factor S were not available from the data gathered in the physical experiments. Here, for simplicity S is assumed to be 0, i.e., none of the kinetic energy associated with the component of the velocity normal to the ramp was converted into gravitational potential energy, while optimised values for the remaining two parameters giving the best fit with the observed experimental data points were found to be ΔE_{gain} = 0.526 Jm^{-3} and F_{ave}= 0.440 Nm^{-3} (**Fig. 5A**). A contour map of the modelled normalised H_{max}/h, as a function of the flow incidence angle onto the slope (φ) and the angle of slope gradient (θ), using the input values above is given in **Figure 5B**.

Overall, our numerical model captured the first-order dependence of normalised maximum run-up height as a function of flow incidence angle and slope gradient (**Fig. 5**), with an R^2 value of 0.764. A critical slope gradient θ exists (θ = 34.5°), where H_{max}/h reaches its maximum value of 2.66. This is approximately consistent with the experimental observations of higher H_{max}/h for a slope of 30° compared to that of 20° and 40° in an oblique setting (**Fig. 3J**). Additionally, when the slope gradient is set to a constant, the normalised maximum run-up height increases with a higher flow incidence angle, consistent with the observed positive relationship between values H_{max}/h versus the flow incidence angle in our physical experiments (**Fig. 3I**).

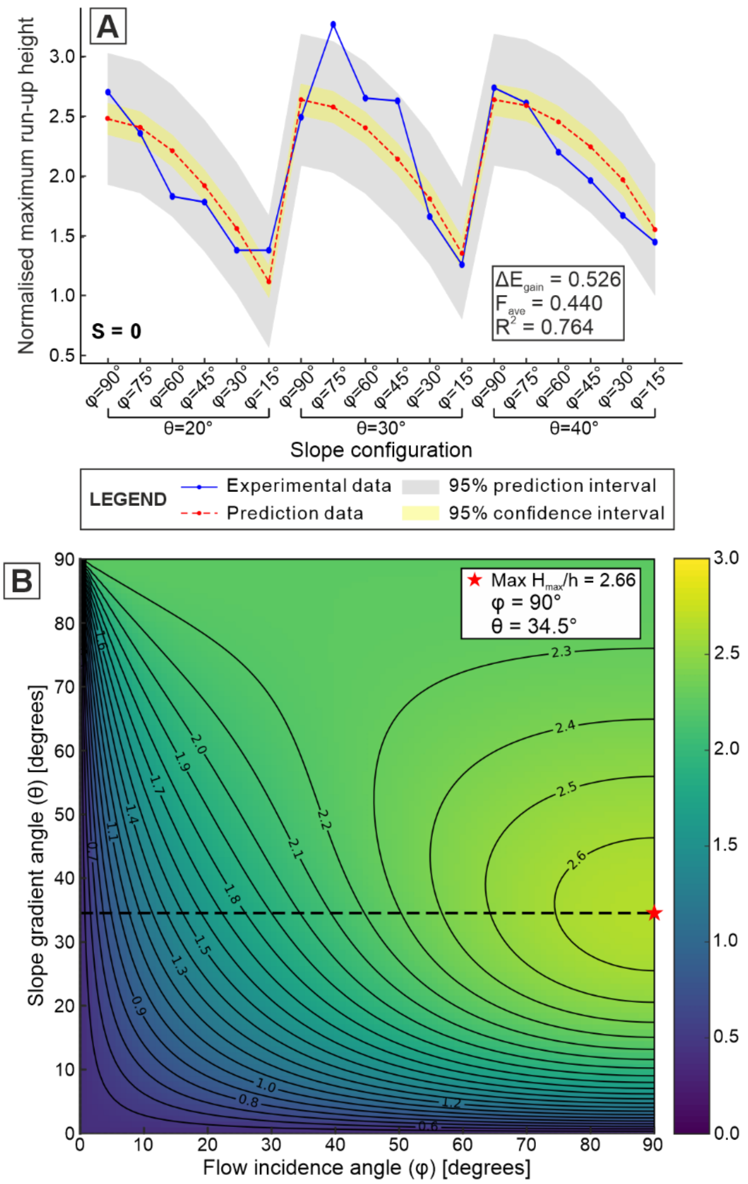

Fig. 5. (A) Comparison between observed and predicted values of normalised maximum run-up height upslope for our 18 ramp experiments. The best-fit values of ΔE_{gain} and F_{ave} in Equation 3 optimised for the observed experimental data points and the fit accuracy (R^2) are given in the bottom right box. The input quantities in the model are set to constant, representative for the current physical experiments in the first 5 s after the current head (z = 0.045 m, ρ_z = 999.8 kg/m^3, $\Delta\rho_z$ = 0.22 kg/m^3, h = 0.11 m, u = 0.0243 m/s). (B) Contour map of modelled normalised maximum run-up height, H_{max}/h, as a function of the flow incidence angle onto the slope (φ) and slope gradient (θ), with the input variables set to constant values typical of current physical experiments and the optimised ΔE_{gain} and F_{ave}.

Evaluation of numerical model by field data

To simulate the normalised maximum run-up height, we assume that the turbidity current is relatively dilute (ρ_s = 1,060 kg/m^3; $\Delta\rho_s$ = 30 kg/m^3) and has an initial downstream velocity of 5 m/s and flow height of 39 m. The energy gain from the internal pressure of the nearby fluid parcels is poorly known, ΔE_{gain} = 9600 Jm^{-3}, is chosen as it is tested to yield an approximately realistic output of (normalised) maximum run-up height. The averaged dissipative force can be approximated as $F_{ave} = \mu N$, where μ is the coefficient of friction and N is the normal contact force from the ramp, which should be equal to the component of the weight normal to the ramp: $N = \rho g' \cos\theta$. Here F_{ave} varies from 0 to 300 Nm^{-3}, approximately corresponding to the case whereby the frictional coefficient μ = 0, 0.001, 0.005 (base-case), 0.01, 0.1, 0.2, 0.3, 0.4, 0.5, 0.6, 0.7 and 1, respectively. These input quantities are chosen arbitrarily but ensuring that they are within ranges of observations from field-scale turbidity currents (e.g., Sinclair, 2000; Mohrig and Buttles, 2007; Symons et al., 2017; Azpiroz-Zabala et al., 2017; Straub et al., 2008; Lamb et al., 2008).

We first conducted sensitivity analysis to explore the effect of different variables incorporated in Equation 3 on the normalised maximum run-up height for a specific topographic configuration (take θ = 45° and φ = 90° for an example) with the above-mentioned input variables set as a base case and S equal to 0.5 (**Fig. S4**). Results indicate that initial downstream flow velocity U and excess density difference $\Delta\rho_s/\rho_s$ are the most influential factors affecting H_{max}/h, collision factor S and energy gain from internal pressure of nearby fluid parcels ΔE_{gain} are moderately sensitive while the averaged dissipative force F_{ave} has the least impact. An inverse relationship is identified between excess density difference or averaged dissipative force F_{ave} versus H_{max}/h, as one would expect, whereas a positive relationship is seen between other input parameters versus H_{max}/h.

We then explored the effect of the flow incidence angle onto the slope (φ) and the angle of slope gradient (θ) on (normalised) maximum run-up height with covarying averaged dissipative force F_{ave} (**Fig. 6**). Taking F_{ave} = 3 Nm^{-3} for example, results indicate that an increase in flow incidence angle with the same slope gradient notably contributes to a higher H_{max}/h. This is because higher incidence angles correspond to better alignment between the average flow velocity and the updip direction. However, the impact of slope gradient is more complicated. A critical angle of slope gradient exists where the normalised H_{max}/h achieves its maximum. For a given incidence angle, increasing the slope gradient will first lead to an increase in the normalised H_{max}/h, which is followed by an ultimate decrease.

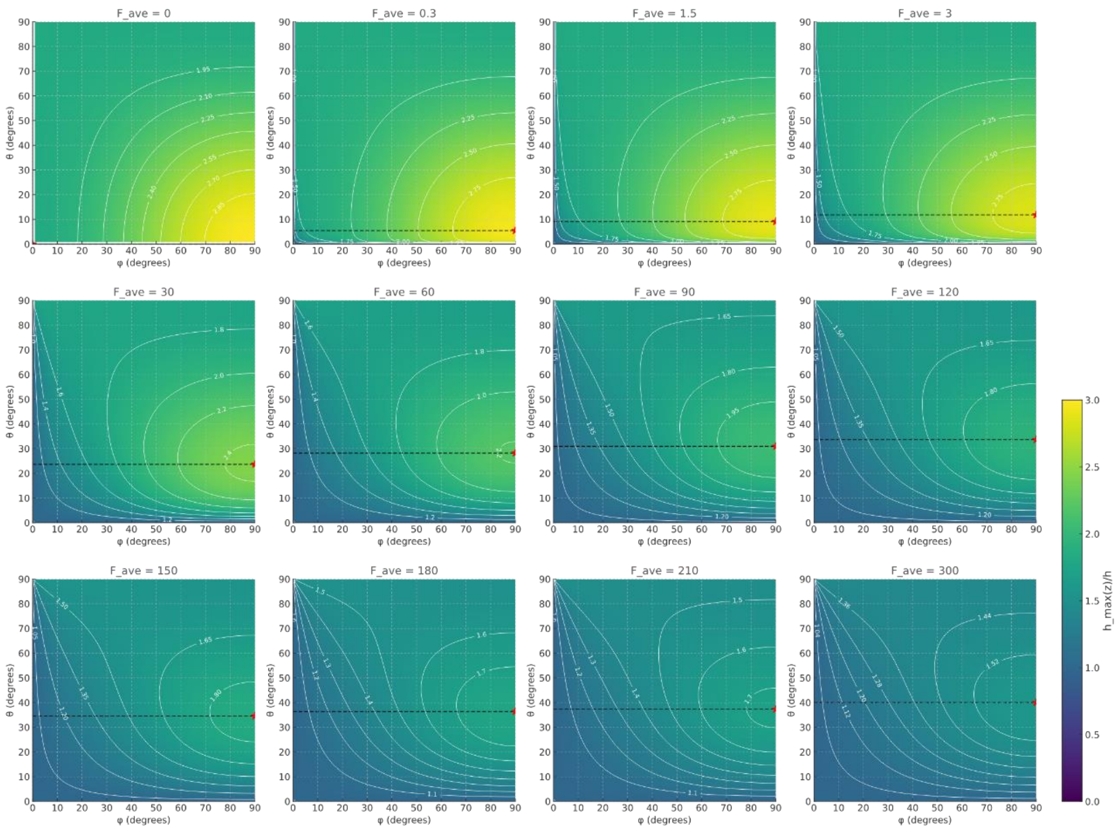

Fig. 6. Numerical model results for the normalised maximum run-up height of turbidity currents interacting with a topographic slope with varying averaged dissipative force F_{ave}. In each panel map, contours of normalised maximum run-up height, H_{max}/h, as a function of the flow incidence angle onto the slope (φ) and the angle of slope (θ), with other variables set to

constant values typical of field-scale turbidity currents (z = 39 m, ρ_z = 1,060 kg/m^3; $\Delta\rho_z$ = 30 kg/m^3; h = 39 m; u_z= 5 m/s). For all panel maps, $S = 0$ assuming a maximal collision model and ΔE_{gain} = 9600 Jm^{-3}. Across the panel maps, the given value of the averaged dissipative force F_{ave}varies from 0 to 300 Nm^{-3}, approximately corresponding to the case whereby the frictional coefficient μ = 0, 0.001, 0.005, 0.01, 0.1, 0.2, 0.3, 0.4, 0.5, 0.6, 0.7 and 1, respectively. Red star denotes the position whereby H_{max}/h reaches its maximum value for a specific topographic configuration with a critical angle of θ and φ.

DISCUSSION

Comparison with existing numerical models

Our experimental results clearly demonstrate that the existing predictive models, including those by Kneller and McCaffrey (1999) and Muck and Underwood (1990), based on simplified 2D settings and orthogonal interactions, underestimate the run-up height for unconfined turbidity currents (**Fig. 3I**). The existing models neglects key factors in 3D unconfined settings, such as lateral flow expansion and divergence on the slope surface, vertical and cross-stream velocity components' contribution to initial kinetic energy and the energy gain from the internal pressure of nearby fluid parcels. Crucially, our experimental data show that maximum run-up heights are influenced not just by the gradient of the topographic slope but also by the angle of incidence of the flow against the slope (see subsection below). These factors are integral to the behaviour of 3D unconfined turbidity currents in natural submarine environments.

Influence of slope gradient and flow incidence angle on the magnitude of maximum run-up height

A key finding from our laboratory experiments is the nonlinear relationship between slope gradient and maximum run-up height (**Fig. 3**). While conventional wisdom suggests that steeper slopes should yield higher run-up heights, we observed that intermediate slopes (around 30°) often exhibited the highest run-up heights compared to both gentler and steeper slopes, particularly in oblique flow configurations. This is further supported by our numerical model predictions (**Fig. 5-6**), which reveal a critical slope gradient θ_c for non-zero average dissipative force F_{ave}, with θ_c increasing with rising F_{ave} (**Fig. 6**). This complicated θ dependence is ascribed to the competition between the following opposite effects: (1) a greater θ means less alignment between the average flow direction and the up-dip direction, lowering the run-up height (**Fig. 4C**); (2) a greater θ also means less overall distance to travel on the slope surface to achieve the same vertical run-up height, which means less energy lost to friction or turbulent dissipation, increasing the run-up height. In the regime $\theta < \theta_c$ with the same flow incidence angle relative to the slope, the influence of the average dissipative force dominates and thus a steeper slope gradient is associated with higher H_{max}/h. In the regime $\theta > \theta_c$ with the same flow incidence angle relative the slope, the influence of the collision factor dominates and thus a steeper slope gradient is associated with lower H_{max}/h.

The flow incidence angle impacts the maximum run-up height markedly. Notably more oblique flow interactions with the topographic slope (e.g., 15°–45° incidence angles) tend to have lower maximum run-up heights due to a lower degree in topographic containment and reduced up-dip velocity component, while near-perpendicular interactions (e.g., 75°–90°) allow more initial kinetic energy to be converted into gravitational potential energy. Importantly, experimental results (**Fig. 3I**) indicate that occasionally, a critical flow incidence angle φ_c exists near the frontal setting, that is, an incidence angle less than 90° at which there is a pronounced boost in superelevation, leading to the greatest value of all the vertical run-ups. This is likely a consequence of variations in the cross-stream velocity component, which effectively change the local incidence angle of the fluid parcel relative to the ramp, locally increasing the incidence angle by a shift $\Delta\varphi$ so that its maximum occurs when $\varphi + \Delta\varphi = 90°$, instead of when $\varphi = 90°$ (the value at which the H_{max}/h would usually reach its maximum). With sufficient data, a more sophisticated version of the predictive model could take into account the cross-stream velocity component and its lateral profile, to facilitate a prediction of this shift and the resulting critical angle φ_c.

Implications for the stratigraphic record

Our results can be used to inform the position of deposition along intrabasinal slopes, and the style of onlap, in the ancient rock record. A lower flow incidence angle onto the slope leads to a lower maximum run-up distance, and an initial increase and subsequently a decrease in the rugosity of the maximum run-up line. A steeper slope results in a shorter maximum run-up distance.

Superelevation of turbidity currents and deposition higher on topographic slopes have been recognized in laboratory (e.g., Muck and Underwood, 1990; Soutter et al., 2021; Keavney et al., 2024), field (e.g., Damuth and Embley, 1979; Cita et al., 1984; Dolan et al., 1989) and outcrop investigations (e.g., Al A'Jaidi et al. 2004; Soutter et al., 2019). Based on experimental observations of unconfined turbidity currents interacting with orthogonal topography, Keavney et al. (2024) pointed out that once the flow encounters the topography, the initial flow decouples: a basal dense region and an upper dilute region. The basal dense part of the flow decelerates quickly at the base of the slope and leads to coarse-grained sediment deposition lower on the slope, and therefore contributes to abrupt pinchouts. The upper dilute part would travel further and deposit finer-grained sediments higher on slopes, and therefore contributes to draping pinchouts. Here, our results support this model and further expand on the characteristics of run-up elevation on slopes, including the magnitude of run-up height and lateral variability in strike direction (**Fig. 7**), which would provide key insights into the 3D stratal onlap termination styles in the ancient rock record.

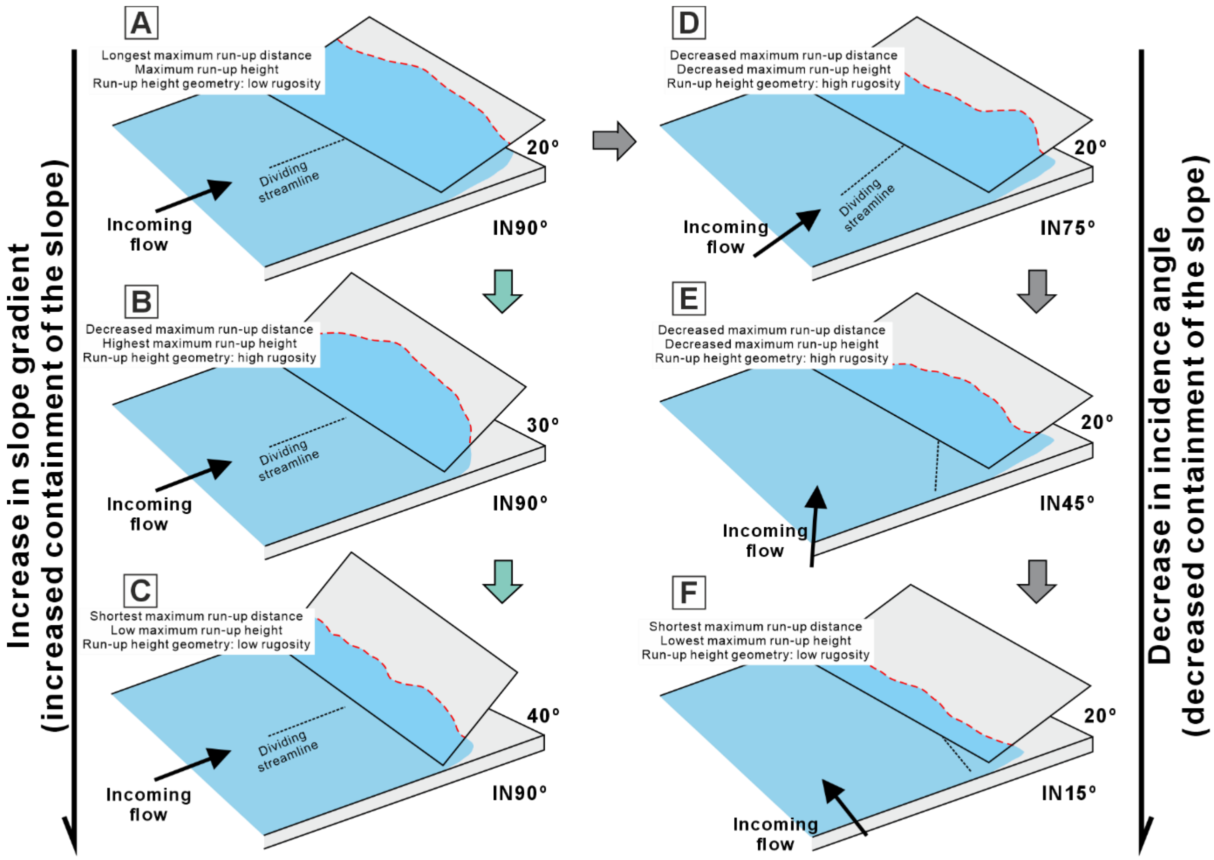

Fig. 7. Schematic diagram illustrating the characteristics of maximum run-up height potential of turbidity currents that interact with different configurations of topographic slopes, including incidence angle of the flow onto the slope (A, D-F) and slope gradient (A-C). The red dashed line indicates the outline of the run-up line on the slope surface. The red filled circle denotes the position of the maximum run-up point.

In a low-gradient and nearly frontal intrabasinal slope, the onlap style in dip section is consistent with the model proposed by Keavney et al. (2024). The upper deposit limit of finer-grained sediments is evenly distributed. In a low-gradient and oblique intrabasinal slope, the upper limit of finer-grained sediments is more laterally variable, but the highest point on slope surface is lower on slopes in a dip direction. In a low-gradient and nearly parallel intrabasinal slope, weak flow stripping would lead to the deposition of a limited zone of draped fines, which abruptly terminates lower on the slope. The upper limit line of the abrupt pinch out in strike direction would exhibit minimal lateral variability. In a steep-gradient and nearly frontal intrabasinal slope, strong topographic containment would lead to a rapid deceleration of the flow. This could lead to the deposition of thick coarser-grained sediments, abruptly terminating lower on slopes, and evenly distributed in a strike direction. Crucially, the nonlinear relationship between slope gradients and flow incidence angles versus maximum run-up heights, i.e., critical slope gradients and flow incidence angles exist which can generate the highest run-up heights, means that a specific topographic configuration exists where the upper limit of the finer-grained sediment reaches its maximum.

The depositional model herein suggests that distinct 3D onlap styles on slopes correspond to different topographic configurations, which can be used to reconstruct the orientation and slope gradient of the topographic slopes in the modern field and ancient rock record. Notably, the maximum run-up distance is a good indicator of topographic configurations; however, the maximum run-up elevation and the geometry of the run-up line do not exhibit the same level of indicative reliability.

Implications for hazard management in natural submarine systems

These findings have important implications for predicting sediment transport and deposition patterns in natural submarine environments. The ability of turbidity currents to climb topographic barriers and deposit material at elevated locations is critical for understanding the distribution of sediments, microplastics, and pollutants on the seafloor. Our results suggest that in regions with varied topography, sediment deposition could occur at higher elevations than previously anticipated, especially when turbidity currents interact with slopes at specific incidence angles and slope gradients.

In the context of deep-sea infrastructure, such as pipelines and communication cables, our findings raise concerns about the potential for greater-than-expected sediment deposition on elevated terrain, which could pose a hazard to these structures. Understanding the dynamics of turbidity current run-up and deposition is therefore crucial for risk assessment and mitigation strategies in such environments.

CONCLUSIONS

This study advances our understanding of the characteristics of maximum run-up height potential (with a focus on the magnitude) of turbidity currents interacting with topographic slopes with varying slope gradients and flow incidence angles onto the slope, in unconfined, 3D settings. Our experimental results show that existing predictive models based on 2D confined flows and frontal topographic configurations markedly underestimate the run-up heights of turbidity currents, highlighting the importance of considering lateral flow expansion and divergence, vertical and/or downstream velocity components and the energy gain from the internal pressure of nearby fluid parcels. Experimental results also highlight the importance of slope gradient and flow incidence angle in controlling the magnitude of maximum run-up height, revealing that intermediate slope gradients (ca. 30°) and (near-)perpendicular flow incidence angles generate the highest run-up heights. Our newly developed numerical model captures the key dynamics of turbidity current interaction with topography in 3D, unconfined settings and provides relatively more accurate predictive framework for run-up heights. These findings are critical for improving sediment transport models, predicting the distribution of sediments, pollutants, and organic carbon in deep-sea environments, assessing seafloor geohazards, and reconstructing ancient deep-water basin palaeogeographies.

MATERIALS AND METHODS

Experimental design and data collection

Details and video of our experiments, performed at the Sorby Environmental Fluid Dynamics Laboratory, University of Leeds, using a large flume tank (10 m long, 2.5 m wide and 1 m deep; **Fig. 2A**) are presented in the **Supporting Information 1** and are summarized here. The tank configuration mirrored previous studies (e.g., Keavney et al., 2024; Wang et al., 2024) and included a 1.8 m long straight input channel section centred at the upstream end of the main tank and a flat basin floor (**Fig. 2A**). Nineteen experiments were performed in total: the first, an unconfined experiment, served as a base case for scaling, while the other eighteen involved a non-erodible smooth planar ramp (1.5 m wide, 1.2 m long) centrally placed in the tank with the ramp's leading edge positioned 3 m downstream from the channel mouth (**Fig. 2A**). Each ramp experiment used a different combination of ramp slope gradient (20°, 30° and 40°) and incidence angle relative to the incoming flow (90°, 75°, 60°, 45°, 30° and 15°; **Fig. 2B**). The tank was filled up to 0.6 m water level with fresh tap water prior to each experiment. During each experimental run, a saline solution of excess density 2.5% (1,025 kg m^{-3}) was pumped at a constant discharge rate of 3.6 L s^{-1} from the mixing tank (**Fig. 2A**). This setup could better constrain the flow thickness, vertical velocity profile and concentration profile of the density current at the base of the barrier ramp (**Fig. 2C**) and hence ensured subcritical, fully turbulent flow conditions (Densimetric Froude number Fr_d = 0.50; Reynolds number Re = 3203; see details in Keavney et al., 2024 and Wang et al., 2024) at the base of the barrier ramp. This can better approximate basin-floor flows in the field which have passed through the channel-lobe transition zone, experiencing a loss in flow confinement (Komar, 1971; Hodgson et al., 2022; Keavney et al., 2024). Each experimental run lasted 130 seconds in total.

In the unconfined experiment, velocity and density profiles over height were recorded for flows at 3 m downstream from the channel mouth along the channel-basin centreline (i.e., the position of the central base of the barrier ramp in subsequent ramp experiments; **Fig. 2A**). These were achieved through the measurements by an Ultrasonic Velocity Profiler (UVP), Acoustic Doppler Velocimeter (ADV) and siphoning system, respectively (see Keavney et al., 2024 and Wang et al., 2024 for details of the UVP, ADV and siphon set-ups; **Fig. S1**). Time-averaged UVP downstream velocity profile and density profile for the flow body at this point (**Fig. 2C-D**) were obtained by averaging measurements over 30 seconds, starting 5 seconds after the current head passed. In the ramp experiments, Pliolite and a small amount of white paint were added to the inlet flow to better visualise the internal fluid motion within the current (cf. Edwards et al., 1994), while fluorescent yellow dye was injected via a series of tubes mounted from the rear of the ramp and flush with its surface, to aid in the visualisation of the density current interacting with the ramp. We used four high-resolution video cameras (GoPro HERO 10; GoPro Inc., USA) to record the flow process in each ramp experiment and finally captured the maximum run-up elevation and the outlines of the maximum run-up geometry on the slope surface from the video stills.

Numerical simulations

To better capture the multidirectional flow-topographic slope interactions in 3D, unconfined settings observed in our physical experiments, we developed a novel numerical model (**Supporting Information 4**) that incorporates the effects of slope gradient angle (θ) and flow incidence angle (φ). The model is also a further development of the Kneller and McCaffrey (1999)'s approach based on energy balance principles, accounting for kinetic energy, potential energy, work done by internal pressure from nearby fluid parcels, as well as frictional and turbulent dissipation.

ACKNOWLEDGEMENTS

This research forms a part of the LOBE 3 consortium project, based at University of Leeds and University of Manchester. The authors thank the sponsors of the LOBE 3 consortium project for financial support: Aker BP, BHP, BP, Equinor, HESS, Neptune, Petrobras, PetroChina, Total, Vår Energi and Woodside. Prof. Chris Paola, Dr. Han Liu based at St. Anthony Falls Laboratory, University of Minnesota and Prof. Ben Kneller based at University of Aberdeen, are thanked for providing some inspirations for the designing of the analytical model shown in this work.

NOMENCLATURE

E: Frictional coefficient

Fr: Froude number

Fr_d: Densimetric Froude number

g: Acceleration due to gravity (m s^{-2})

H_{max}: Maximum run-up height on slopes (m)

h_{max}: Maximum run-up height on slopes for a specific parcel of the fluid (m)

h: Flow height (m)

h_p: Height of the maximum downstream velocity above the basin floor (m)

L_{max}: Maximum run-up distance on slopes (m)

Re: Reynolds number

U: Mean depth-averaged downstream velocity (m s^{-1})

u_p: Maximum downstream velocity (m s^{-1})

u_z: Velocity component at initial height z that is normal to the topography (m s^{-1})

z: Initial height of a specific parcel of the fluid (m)

ρ_s: Mean depth-averaged density of the current (kg m^{-3})

$\Delta\rho_z$: Density difference between the fluid at initial height z and the ambient fluid (kg m^{-3})

DATA AVAILABILITY STATEMENT

The data that support the findings of this study are available from the corresponding author upon reasonable request.

REFERENCES

Al Ja'Aidi, O.S., **McCaffrey, W.D.** and **Kneller, B.C.** (2004) Factors influencing the deposit geometry of experimental turbidity currents: implications for sand-body architecture in confined basins. In: *Confined Turbidite Basins* (Eds S.A. Lomas and P. Joseph), *Geol. Soc. London. Spec. Publ.*, **222**, 45–58.

Allen, J.R.L., 1985, Principles of Physical Sedimentology. George Allen &Unwin, London, 223-242pp.

Apps, G.M., **Peel, F.J.**, **Travis, C.J.** and **Yielding, C.A.** (1994) Structural controls on Tertiary deep water deposition in northern Gulf of Mexico. SEPM, Gulf Coast Section Meeting, Houston, Proceedings, pp. 1–7.

Bell, D., Stevenson, C.J., Kane, I.A., Hodgson, D.M. and **Poyatos-Moré, M.** (2018) Topographic controls on the development of contemporaneous but contrasting basin-floor depositional architectures. *J. Sed. Res.*, **88**, 1166-1189.

Bruschi, R., **Bughi, S.**, **Spinazzè, M.**, **Torselletti, E.** and **Vitali, L.** (2006) Impact of debris flows and turbidity currents on seafloor structures. *Norwegian J. Geol.*, **86**, 317–336.

Carter, L., **Gavey, R.**, **Talling, P.** and **Liu, J.** (2014) Insights into submarine geohazards from breaks in subsea telecommunication cables. *Oceanography*, **27**, 58–67.

Cita, M., **Beghi, C.**, **Camerlenghi, A.**, **Kastens, K.**, **McCoy, F.**, **Nosetto, A.**, **Parisi, E.**, **Scolari, F.** and **Tomadin, L.** (1984) Turbidites and megaturbidites from the Herodotus abyssal plain (eastern Mediterranean) unrelated to seismic events. *Mar. Geol.*, **55**, 79-101.

Damuth, J.E. and **Embley, R.W.** (1979) Upslope flow of turbidity currents on the northwest flank of the Ceara Rise, Western equatorial Atlantic. *Sedimentology*, **26**, 825-834.

Dolan, J.F., **Beck, C.** and **Ogawa, Y.** (1989) Upslope deposition of extremely distal turbidites: An example from the Tiburon Rise, west-central Atlantic. *Geology*, **17**, 990-994.

Dzulynski, S., **Ksiazkiewicz, M.** and **Kuenen, P. H.** (1959) Turbidites in flysch of the Polish Carpathian Mountains. *Geol. Soc. Am. Bull.*, **70**, 1089-1118.

Edwards, D.A., Leeder, M.R., Best, J.L. and **Pantin, H.M.** (1994) On experimental reflected density currents and the interpretation of certain turbidites. *Sedimentology*, **41**, 437-461.

Haward, M. (2018) Plastic pollution of the world's seas and oceans as a contemporary challenge in ocean governance. *Nat. Commun.*, **9**, 667.

Kane, I.A., **Clare, M.A.**, **Miramontes, E.**, **Wogelius, R.**, **Rothwell, J.J.**, **Garreau, P.** and **Pohl, F.** (2020) Seafloor microplastic hotspots controlled by deep-sea circulation. *Science*, **368**, 1140-1145.

Keavney, E., **Peakall, J.**, **Wang, R.**, **Hodgson, D.M.**, **Kane, I.A.**, **Keevil, G.M.**, **Brown, H.C.**, **Clare, M.A.** and **Hughes M.** (2024) Flow evolution and velocity structure of unconfined density currents interacting with frontally containing slopes. *EarthArxiv,* doi: 10.31223/X5CM35.

Kneller, B. and **Buckee, C.** (2000) The structure and fluid mechanics of turbidity currents: a review of some recent studies and their geological implications. *Sedimentology*, **47**, 62-94.

Kneller, B. and **McCaffrey, W.** (1999) Depositional effects of flow nonuniformity and stratification within turbidity currents approaching a bounding slope: deflection, reflection, and facies variation. *J. Sed. Res*., **69**, 980-991.

Komar, P.D. (1969) The channelized flow of turbidity currents with application to Monterey deep-sea fan channel. *J. Geophys. Res.*, **74**, 4544-4558.

Kuenen, P.H. and **Migliorini, C.I.** (1950) Turbidity currents as a cause of graded bedding. *J. Geol.*, **58**, 91–127.

Lamb, M.P., **Parsons, J.D.**, **Mullenbach, B.L.**, **Finlayson, D.P.**, **Orange, D.L.** and **Nittrouer, C.A.** (2008) Evidence for superelevation, channel incision, and formation of cyclic steps by turbidity currents in Eel Canyon, California. *Geol. Soc. Am. Bull.,* **120**, 463-475.

Lane-Serff, G.F., **Beal, L.M.** and **Hadfi eld, T.D.** (1995) Gravity current flow over obstacles. *J. Fluid Mech.*, **292**, 39–54.

Lomas, S.A. and **Joseph, P.** (2004) Confined turbidite systems. In: *Confined Turbidite Systems* (Eds S.A. Lomas, P. Joseph), *Geol. Soc. Spec. Publ.*, **222**, 1-7.

Marshall, C.R., Dorrell, R.M., Keevil, G.M., Peakall, J. and **Tobias, S.M.** (2023) On the role of transverse motion in pseudo-steady gravity currents. *Exp. Fluids*, **64**, 63.

Muck, M.Y. and **Underwood, M.B.** (1990) Upslope flow of turbidity currents: A comparison among field observations, theory, and laboratory methods. *Geology*, **18**, 54–57.

Nomura, S., **Hitomi, J.**, **De Cesare, G.**, **Takeda, Y.**, **Yamamoto, Y.** and **Sakaguchi, H.** (2019) Sediment mass movement of a particle-laden turbidity current based on ultrasound velocity profiling and the distribution of sediment concentration. *Geol. Soc. Spec. Publ.*, **477**, 427-437.

Normark, W.R. (1985) Local morphologic controls and effects of basin geometry on flow processes in deep marine basins. In: *Provenance of Arenites* (Ed G.G. Zuffa), Dordrecht, Netherlands, D. Reidel, pp. 47–73.

Normark, W.R., **Posamentier, H.** and **Mutti, E.** (1993) Turbidite systems: state of the art and future directions. *Rev. Geophys.*, **31**, 91-116.

Pantin, H.M. and **Leeder, M.R.** (1987) Reverse flow in turbidity currents: the role of internal solitons. *Sedimentology*, **34**, 1143-1155.

Patacci, M., Haughton, P.D.W. and **McCaffrey, W.D.** (2015) Flow behaviour of ponded turbidity currents. *J. Sed. Res*., **85**, 885-902.

Pirmez, C. and **Imran, J.** (2003) Reconstruction of turbidity currents in Amazon Channel. *Mar. Pet. Geol.*, **20**, 823–849.

Reece, J.K., **Dorrell, R.M** and **Straub, K.M.** (2024a) Circulation of hydraulically ponded turbidity currents and the filling of continental slope minibasins. *Nat. Commun.*, **15**, 2075.

Reece, J.K., **Dorrell, R.M** and **Straub, K.M.** (2024b) Influence of flow discharge and minibasin shape on the flow behavior and depositional mechanics of ponded turbidity currents. *GSA Bulletin*, https://doi.org/10.1130/B37517.1

Rottman, J.W., **Simpson, J.E.** and **Hunt, J.C.R.** (1985) Unsteady gravity current flows over obstacles: some observations and analysis related to the Phase II trials. *J. Hazard. Mater.*, **11**, 325–340.

Sequeiros, O.E., **Spinewine, B.**, **Beaubouef, R.T.**, **Sun, T.**, **Garcia, M.H.** and **Parker, G.** (2010) Bedload transport and bed resistance associated with density and turbidity currents. *Sedimentology*, **57**, 1463-1490.

Sestini G. (1970) Flysch facies and turbidite sedimentology. *Sediment. Geol.*, **4**, 559–597.

Simpson, J.E. (1987) Gravity currents in the environment and the laboratory. Ellis Horwood, Ltd., Chichester, England, 244 pp.

Sinclair, H.D. (1994) The influence of lateral basinal slopes on turbidite sedimentation in the Annot Sandstones of SE France. *J. Sediment. Res.*, **64**, 42–54.

Soutter, E.L., **Kane, I.A.**, **Fuhrmann, A.**, **Cumberpatch, Z.A.** and **Huuse, M.** (2019) The stratigraphic evolution of onlap in clastic deep-water systems: autogenic modulation of allogenic signals. *J. Sediment. Res.*, **89**, 890–917.

Soutter, E.L., Bell, D., Cumberpatch, Z.A., Ferguson, R.A., Spychala, Y.T., Kane, I.A. and **Eggenhuisen, J.T.** (2021) The influence of confining topography orientation on experimental turbidity currents and geological implications. *Front. Earth. Sci*., **8**. 540633.

Straub, K.M., **Mohrig, D.**, **McElroy, B.**, **Buttles, J.** and **Pirmez, C.** (2008) Interactions between turbidity currents and topography in aggrading sinuous submarine channels: A laboratory study. *Geol. Soc. Am. Bull.*, **120**, 368-385.

Tinterri, R. (2011) Combined flow sedimentary structures and the genetic link between sigmoidal- and hummocky-cross stratification. *GeoActa*, **10**, 43-85.

Tinterri, R., Mazza, T. and **Muzzi Magalhaes, P.** (2022) Contained-reflected megaturbidites of the Marnoso-arenacea Formation (Contessa Key Bed) and Helminthoid Flysches (Northern Apennines, Italy) and Hecho Group (South-Western Pyrenees). *Front. Earth. Sci*., **25**, 817012.

Wang, R., **Peakall, J.**, **Hodgson, D.**, **Keavney, E.**, **Brown, H.** and **Keevil, G.** (2024) Unconfined turbidity current interactions with oblique slopes: deflection, reflection and combined-flow behaviours. *EarthArxiv*, doi: 10.31223/X5569F.

Wei, T., **Peakall, J.**, **Parsons, D.R.**, **Chen, Z.**, **Zhao, B.** and **Best, J.L.** (2013) Three-dimensional gravity-current flow within a subaqueous bend: Spatial evolution and force balance variations. *Sedimentology*, **60**, 1668–1680.

Wynn, R.B., **Talling, P.J.**, **Masson, D.G.**, **Stevenson, C.J.**, **Cronin, B.T.** and **Bas, T.L.** (2010) Investigating the timing, processes and deposits of one of the World's largest submarine gravity flows: the 'Bed 5 Event' off Northwest Africa. In: *Submarine mass movements and their consequences* (Eds D.C. Mosher, R.C. Shipp, L. Moscardelli, J.D. Chaytor, C.D.P. Baxter and H.J. Lee, R. Urgeles), Springer, Dordrecht, Netherlands, pp. 463-474.

SUPPLEMENTARY TEXT

Supporting Information 1: Physical experiments

Experiments were carried out in the Sorby Environmental Fluid Dynamics Laboratory, University of Leeds, using a large flume tank (10 m long, 2.5 m wide and 1 m deep; **Fig. 2A**). The tank configuration mirrored previous studies (e.g., Keavney et al., 2024; Wang et al., 2024) and included a 1.8 m long straight input channel section centred at the upstream end of the main tank and a flat basin floor (**Fig. 2A**). Nineteen experiments were performed in total: the first, an unconfined experiment, served as a base case for scaling, while the other eighteen involved a non-erodible smooth planar ramp (1.5 m wide, 1.2 m long) centrally placed in the tank with the ramp's leading edge positioned 3 m downstream from the channel mouth (**Fig. 2A**). Each ramp experiment utilised a different combination of incidence angle relative to the incoming flow (i.e., 90°, 75°, 60°, 45°, 30° and 15°; **Fig. 2B**) and ramp slope gradient (i.e., 20°, 30° and 40°).

The tank was filled up to 0.6 m water level with fresh tap water prior to each experiment. During each experimental run, a saline solution of excess density 2.5% (1,025 kg m^{-3}) was pumped at a constant discharge rate of 3.6 L s^{-1}, flowing from the mixing tank where the saline solution was mixed, through the straight channel section onto the basin floor. This setup tightly controlled the flow thickness, vertical velocity profile and concentration profile of the density current at the base of the barrier ramp (**Fig. 2C**) and hence ensured subcritical, fully turbulent flow conditions (Densimetric Froude number $Fr_d = 0.50$; Reynolds number $Re = 3203$; see details in Keavney et al., 2024 and Wang et al., 2024) at the base of the barrier ramp, in order to better approximate basin-floor flows in the field which have passed through the channel-lobe transition zone, experiencing a loss in flow confinement (Komar, 1971; Hodgson et al., 2022). Each experimental run lasted 130 seconds in total.

In the unconfined experiment, the inlet flow was dyed purple to aid flow visualisation. Velocity and density profiles over height were recorded for flows at 3 m downstream from the channel mouth along the channel-basin centreline (i.e., the position of the central base of the barrier ramp in subsequent experiments; **Fig. 2A**). These were achieved through the measurements by the Ultrasonic Velocity Profiler (UVP), Acoustic Doppler Velocimeter (ADV) and siphoning system, respectively (see Keavney et al., 2024 and Wang et al., 2024 for details of the UVP, ADV and siphon set-ups; **Fig. S1**). Time-averaged UVP downstream velocity profile and density profile for the flow body at this point (**Fig. 2C**) were obtained by averaging measurements over 30 seconds, starting 5 seconds after the current head passed. In the ramp experiments, Pliolite, a low density and highly reflective polymer (subspherical, mean grain size of 1.5 mm, density of 1050 kg m^{-3}), and a small amount of white paint were added to the inlet flow to better visualise the internal fluid motion within the current (cf. Edwards et al., 1994). Fluorescent yellow dye was injected via a series of tubes mounted from the rear of the ramp and flush with its surface, to aid the visualisation of the density current interacting with the barrier ramp. Each ramp experiment was recorded using up to four high-resolution video cameras (GoPro HERO 10; GoPro Inc., USA) to capture front, side, and top views of the experiment. For each ramp experiment, measurements of the maximum run-up elevation and the outline of the run-up geometry on the barrier ramp were made from the video stills.

Supporting Information 2: Details on the estimation of maximum run-up height based on the Kneller and McCaffrey (1990) model

Based on the unconfined control experiment, the maximum run-up height H_{max} of the experimental flows modelled by the Kneller and McCaffrey (1990) method were estimated using the time-averaged downstream velocity profile of UVP and density profile of the experimental density currents at 3 m downstream from the channel mouth along the channel-basin centreline for the first 5 s after the current head. The first 5 s time window was chosen as it is the dilute head of the density current that appears to mainly contribute to the maximum value of the run-up elevation over the course of the experiment (**Video S1; Fig. S2**). Assuming no frictional energy loss and that the flow strikes the topographic slope with a right incidence angle, results indicate an estimated maximum run-up height of the experimental flows of ca. 0.23 m on the barrier ramp, ca. 2.1 times flow thickness (**Fig. 2C**).

Supporting Information 3: Geometry of maximum run-up line on slopes in the ramp experiments

In contrast to previous studies, these unconfined experiments permit the geometry of the flow front at the maximum run-up height to be documented using video stills, and how this geometry changes through time.

Variation of incidence angles of the current onto the slope

Characteristics on the geometry of the maximum run-up line on slopes as a function of the incidence angle onto the slope are examined for experiments S30°IN90°, S30°IN75°, S30°IN45°, S30°IN30° and S30°IN15° (**Fig. 3B, D-F**). Notably, a lower incidence angle experimental configuration leads to an initial increase in the rugosity of the maximum run-up line on slopes and subsequently a decrease in the rugosity.

Variation of slope gradients

Characteristics on the geometry of the maximum run-up line on slopes as a function of the slope angle of the topographic slope are examined for experiments S20°IN75°, S30°IN75° and S40°IN75° (**Fig. 3A-C**). Notably, the maximum run-up line on the topographic slope for experiment S20°IN75° exhibits no pronounced lateral variability across the slope. In Experiment S30°IN75°, the maximum run-up point resides laterally at ca. 0.37 m away from the right edge of the ramp and the maximum run-up line on the slope displays a high rugosity. Comparatively, the rugosity of the maximum run-up line on a slope of 30˚ is higher than for 20˚ and 40˚ slopes.

Fluctuations of maximum run-up line on slopes

To characterise the fluctuations of maximum run-up line on slopes, we tracked and outlined the run-up line on slopes using a 15 s time window (1 s time interval) after reaching the maximum run-up height for experiments S20°IN75°, S30°IN75° and S40°IN75° (**Fig. 3A-C**). Results indicate that notably, the maximum run-up line on the topographic slope is not stable and fluctuates both vertically and laterally. For instance, in Experiment S40°IN75°, the maximum run-up line can travel up to 0.5 m distance on the slope on the left edge of the ramp (**Fig. 3C**).

Supporting Information 4: Derivation of the numerical model for the estimation of maximum run-up height in an unconfined setting

Our experimental data on observed maximum run-up height (**Fig. 3I**) challenges the application of existing methods for estimating upslope run-up elevation when turbidity currents encounter a frontal topographic slope in an unconfined setting. In this section, we address this issue and introduce a novel numerical model that also incorporates the effects of slope gradient (θ) and flow incidence angle (φ). The model is based on energy balance principles, accounting for kinetic energy, potential energy, work done by pressure, and frictional heat loss in the sedimentary system (Allen, 1985). Between first meeting the ramp and reaching its maximum height, the energy balance equation for a fluid parcel (per unit volume) is expressed as:

$$KE_{inital} + \Delta E_{gain} = KE_{final} + \rho g' \Delta z + \Delta E_{loss} \quad \text{(S1)}$$

where KE_{inital} is the initial kinetic energy of the fluid parcel, ΔE_{gain} is the energy contribution from pressure gradients in the fluid, KE_{final} is the kinetic energy the fluid parcel retains due to its along-strike motion, ρ is the density of the fluid, $g' = g\ \Delta\rho/\rho$ is the reduced gravitational field strength, Δz is the vertical height gain and ΔE_{loss} is the energy lost to friction and/or turbulent dissipation. The fluid parcel here is approximated as retaining its density throughout the run-up, so that the excess density $\Delta\rho/\rho$ remains constant.

The initial kinetic energy can be estimated using trigonometric relationships between velocity components. For simplicity, we work with a horizontally averaged initial downstream velocity $\vec{U} = (u_z, 0, 0)$ for each parcel of fluid meeting the ramp, where the x, y and z axes are aligned with the downstream, cross-stream and vertical directions, respectively (**Fig. 2A**). The velocity can be decomposed into two horizontal components: the horizontal updip component $\vec{U}_{hu}$ with a magnitude of $U \sin \varphi$ and the along-strike component $\vec{U}_{as}$ with a magnitude of $U \cos \varphi$ (**Fig. 4B**). The along-strike component does not contribute to the maximum upslope height H_{max}, since it remains approximately constant throughout the run-up process, meaning its associated kinetic energy $KE_{final} = \frac{1}{2}\rho U^2 \cos^2 \varphi$ can be subtracted from both sides of Equation S1, with any losses absorbed into the ΔE_{loss} term. While the kinetic energy associated with the horizontal updip component is the primary source of the fluid parcel's ultimate gravitational potential energy, some energy dissipation will occur during the initial collision with the ramp surface (**Video S1**). The component of $\vec{U}_{hu}$ that is normal to the ramp, denoted as $\vec{U}_n$, must change direction upon collision with the ramp, so only an unknown fraction of the corresponding kinetic energy will be available to contribute to the maximum run-up elevation. Thus, we further decompose $\vec{U}_{hu}$ into the updip and the normal component: $\vec{U}_{hu} = \vec{U}_u + \vec{U}_n$ (**Fig. 4C**). A dimensionless collision factor S (ranging from 0 to 1) characterises the fraction of the normal component's kinetic energy that contributes to H_{max}. Thus, the kinetic energy from the updip velocity ($\frac{1}{2}\rho U^2 \sin^2 \varphi \cos^2 \theta$) and a fraction S of that from the normal velocity ($\frac{1}{2}\rho U^2 \sin^2 \varphi \sin^2 \theta$) represent the total kinetic energy available for conversion to potential energy. The energy loss ΔE_{loss} is expected to increase with distance and so for simplicity, is herein approximated as work done by an effective average dissipative force, $F_{ave}\Delta D$, where F_{ave} is the average dissipative force per unit volume, acting in the direction opposed to the fluid parcel's velocity and ΔD is the total distance travelled up the slope. Substituting into Equation S1 and subtracting KE_{final} from each side yields:

$$\frac{1}{2}\rho U^2 \sin^2 \varphi \cos^2 \theta + S\left(\frac{1}{2}\rho U^2 \sin^2 \varphi \sin^2 \theta\right) + \Delta E_{gain} = \rho g' \Delta z + \frac{F_{ave}\Delta z}{\sin \alpha} \qquad (S2)$$

where ΔD has been approximated by $\frac{\Delta z}{\sin \alpha}$, with $\alpha = \tan^{-1}(\sin \varphi \tan \theta)$ representing the 'effective slope' of the ramp in the downstream (x) direction in the vertical (x, z) plane (**Fig. 4D**).

The maximum run-up height for a fluid parcel at initial height z is then given by:

$$h_{max}(z) = z + \frac{\frac{1}{2}\rho_z {u_z}^2 \sin^2 \varphi \,(\cos^2 \theta + S \sin^2 \theta) + \Delta \mathrm{E}_{\mathrm{gain}}}{\Delta \rho_z \, g + \frac{F_{ave}}{\sin \alpha}} \quad \text{(S3)}$$

with the z subscripts referring to the density and velocity at height z. The overall H_{max} is the maximum h_{max} for all fluid parcels, and thus occurs when

$$\frac{d}{dz}\left(z + \frac{\frac{1}{2}\rho_z {u_z}^2 \sin^2 \varphi \,(\cos^2 \theta + S \sin^2 \theta) + \Delta \mathrm{E}_{\mathrm{gain}}}{\Delta \rho_z \, g + \frac{F_{ave}}{\sin \alpha}}\right) = 0 \quad \text{(S4)}$$

Therefore, the maximum run-up height H_{max} for the fluid is a function of their measured vertical velocity profile and density profile and hence cannot be completely specified until the velocity and density profiles are known (Kneller and McCaffrey, 1999).

In the limiting case where S = 1 (no energy lost during in the collision with the ramp), Equation S3 simplifies to:

$$h_{max}(z) = z + \frac{\frac{1}{2}\rho_z {u_z}^2 \sin^2 \varphi + \Delta \mathrm{E}_{\mathrm{gain}}}{\Delta \rho_z \, g + \frac{F_{ave}}{\sin \alpha}}$$

For S = 0 (maximal collision loss model), it simplifies to:

$$h_{max}(z) = z + \frac{\frac{1}{2}\rho_z {u_z}^2 \sin^2 \varphi \cos^2 \theta + \Delta \mathrm{E}_{\mathrm{gain}}}{\Delta \rho_z \, g + \frac{F_{ave}}{\sin \alpha}}$$

In frontal settings where φ = 90º, the equation further reduces to:

$$h_{max}(z) = z + \frac{\frac{1}{2}\rho_z {u_z}^2 \cos^2\theta + \Delta \mathrm{E}_{\mathrm{gain}}}{\Delta\rho_z\, g + \frac{F_{ave}}{\sin\alpha}}$$

The model can also be generalised to incorporate initial velocities with significant cross-stream and vertical components, if data is available for these. The initial velocity of the fluid parcel at height z can be generalised to $\vec{U} = (u_z, v_z, w_z)$, where u , v and w are the downstream, cross-stream and vertical velocity components, respectively, which for simplicity are assumed to depend only on z (although in reality these velocity components will depend on x, y too). As before, the predicted run-up height for a fluid parcel at initial height z is

$$h_{max}(z) = z + \frac{\frac{1}{2}\rho_z((U_u(z))^2 + S(U_n(z))^2) + \Delta E_{gain}}{\Delta\rho_z\, g + \frac{F_{ave}}{\sin\alpha}} \quad \text{(S5)}$$

where the various quantities are defined as follows: $U_u(z)$, and $U_n(z)$ are the projections of $\vec{U}$ onto the up-dip direction and the direction normal to the ramp surface, respectively; ΔE_{gain} is the energy gained from internal pressure and interactions of the fluid parcel with neighbouring fluid parcels; S is a dimensionless collision factor ranging from 0 to 1, characterising the fraction of kinetic energy associated with the normal component of the initial velocity that contributes to H_{max}; F_{ave} is the average dissipative force per unit volume, acting in the direction opposed to the fluid parcel's velocity; the angle $\alpha = \tan^{-1}(\sin(\varphi + \beta)\tan\theta)$ represents the 'effective slope' of the ramp in the vertical plane of the initial fluid parcel's initial velocity, and is a function of the overall flow incidence angle φ against the ramp and the slope gradient θ, as well as the angle β between the horizontal component of the fluid parcel's velocity and the overall downstream direction, given by $\beta = \tan(v_z/u_z)$ (**Fig. 4D**). The up-dip and normal projections of the velocity are

$$U_u(z) = (u_z \sin\varphi - v_z \cos\varphi)\cos\theta + w_z \sin\theta$$

$$U_n(z) = -(u_z \sin\varphi - v_z \cos\varphi)\sin\theta + w_z \cos\theta$$

Typically, the downstream velocity profile u_z is more predictable than those of the cross-stream and vertical components, which will vary across the gravity current head, taking a range of positive or negative values, depending on both the degree of lateral flow spreading and unpredictable turbulent fluctuations. As a result, these components may be treated as small fluctuations lying in some range proportional to the downstream velocity, $-\Delta v \leq v_z \leq \Delta v$ and $-\Delta w \leq w_z \leq \Delta w$, with $\Delta v = f_y u_z$ and $\Delta w = f_z u_z$, where f_y and f_z quantify the lateral and vertical variability as a dimensionless fraction of the downstream velocity, respectively (found to be ca. 10% in Nomura et al., 2019; Marshall et al., 2023; Keavney et al. 2024). Then, as before, one can find the maximum run-up height of the turbidity current by finding the maximum value of the function $h_{max}(z)$.

Supporting Information 5: Comparison of the numerical-model predictions with the observed experimental data using 3D velocity components

To test the validity of the numerical model above, its general run-up height predictions are compared to the observed values for each of the 18 ramp experiments herein, with the aim of approximating the overall dependence of (normalised) maximum run-up height on flow incidence angle and slope gradient. Due to the broad approximations made in the model and the turbulent nature of the flow ($Re \approx 3000$), only an approximate fit to the data is to be expected. To be fully realistic would require a Computational Fluid Dynamics simulation, but the purpose here is to provide a method of estimation that can be calculated quickly for practical purposes. Values of the input quantities representative of those measured in the current physical experiments in the first 5 s after the current head were substituted into the model (z = 0.045 m, ρ_z = 999.8 kg/m^3, $\Delta\rho_z$ = 0.22 kg/m^3, h = 0.11 m, u_z= 0.0243 m/s, v_z = -0.12u_z, w_z = 0.09u_z; **Fig. S2**). However, accurate values for the energy gain ΔE_{gain}, averaged dissipative force F_{ave} and collision factor S were not available from the physical experiments. Here, for simplicity the collision factor S is assumed to be 0, i.e., none of the kinetic energy associated with the component of the velocity normal to the ramp was converted into gravitational potential energy, while optimised values for the remaining two parameters giving the best fit with the observed experimental data points were found to be ΔE_{gain} = 0.479 Jm^{-3} and F_{ave} = 0.459 Nm^{-3} (**Fig. S3A**). A contour map of the modelled normalised maximum run-up height, H_{max}/h, as a function of the flow incidence angle onto the slope (φ) and the angle of slope gradient (θ), using the input values above is given in **Figure S3B**.

Overall, our numerical model captured the first-order dependence of normalised maximum run-up height as a function of flow incidence angle and slope gradient (**Fig. 6B**). A critical θ and φ exists (θ = 35.5° and φ = 82.7°), where H_{max}/h reaches its maximum value of 2.58. This is approximately consistent with the experimental observations of higher H_{max}/h for a slope of 30° compared to that of 20° and 40° in an oblique setting (**Fig. 3J**). Additionally, when the slope gradient is set to a value equal to or close to the critical value, the normalised maximum run-up height first increases first with a higher flow incidence angle and then begins to decrease again towards 90°, consistent with the seemingly anomalous low value of H_{max}/h in frontal setting of Experiment 30° (**Fig. 3I**). When the slope gradient is set to a constant deviated from the critical value, the normalised maximum run-up height increases with a higher flow incidence angle, consistent with the observed general positive relationship between values of H_{max}/h versus the flow incidence angle in our physical experiments (**Fig. 3I**).

SUPPLEMENTARY FIGURES AND TABLES

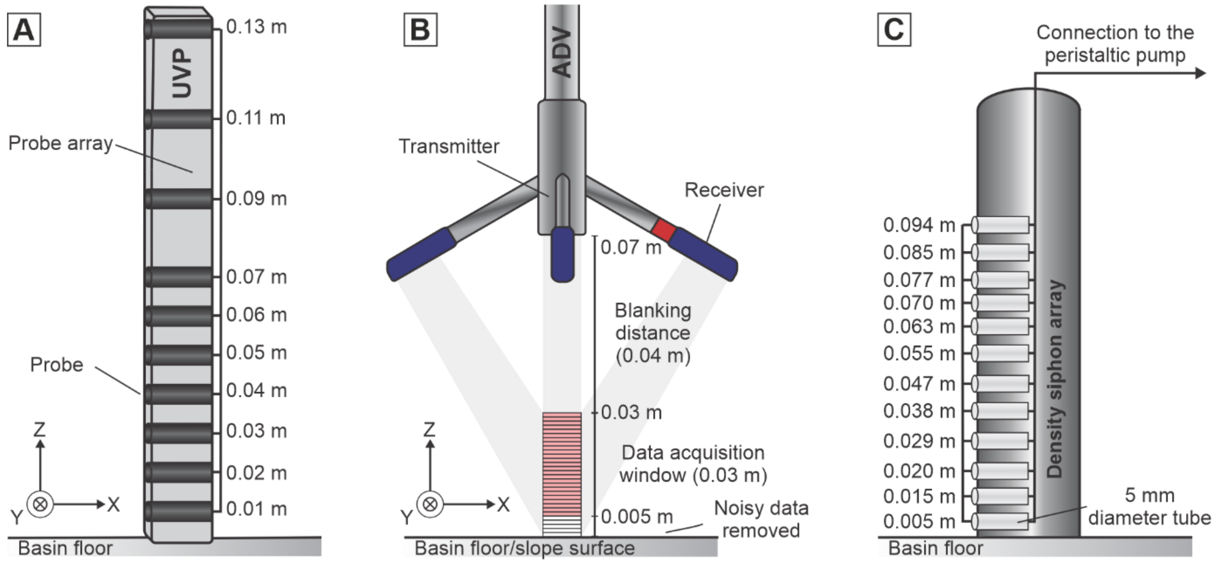

Fig. S1. Set up of (A) the UVP, (B) ADV and (C) siphoning systems in this study to measure the velocity and density profiles, respectively. All profiles were measured vertical to the basin floor, irrespective of whether the instrument was mounted above the basin floor or the slope surface. Modified after Keavney et al. (2024).

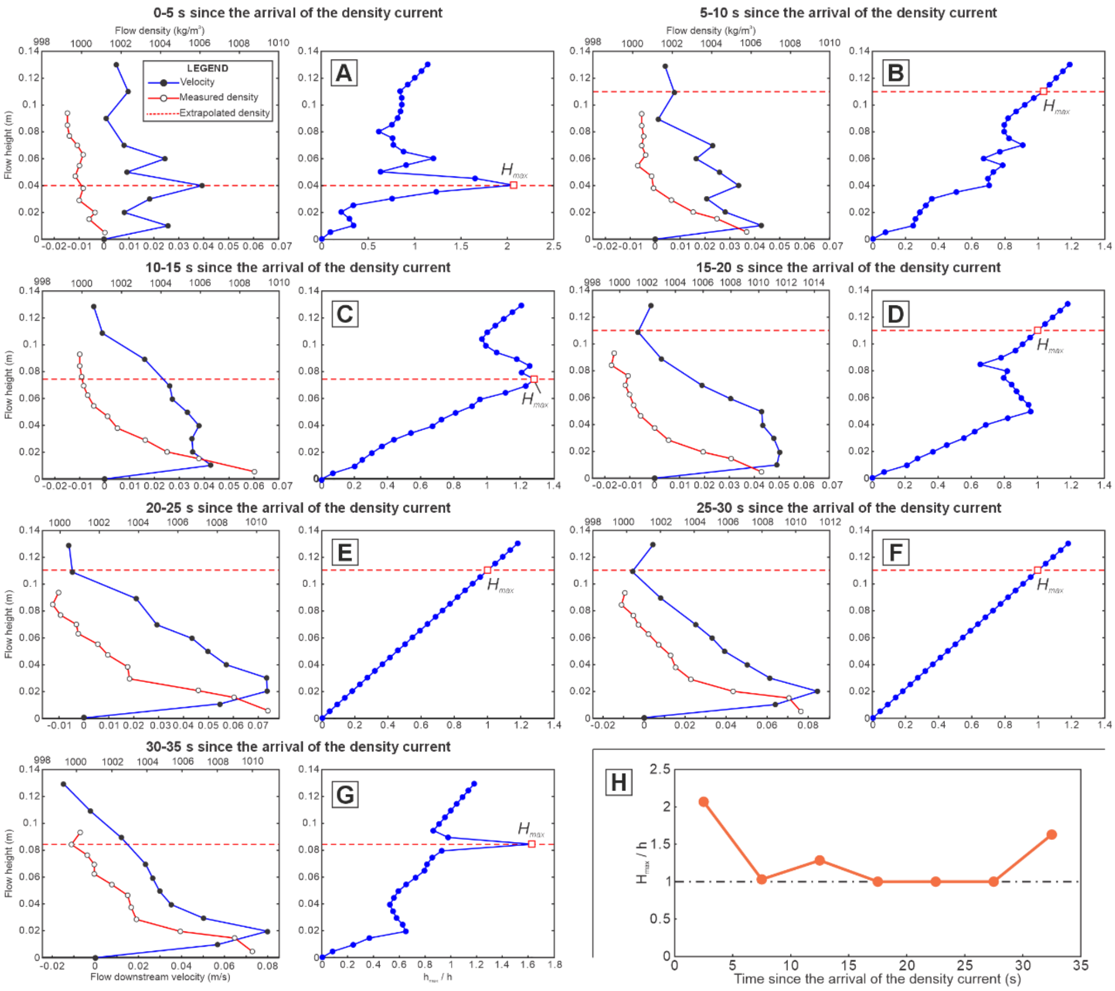

Fig. S2. (A-G) Time-averaged downstream velocity profile of UVP and density profile of the experimental density currents at 3 m downstream from the channel mouth along the channel-basin centreline for the first 35 s (every 5 s time window) after the current head in the unconfined reference experiment. The panel map on the right for each time interval indicates the vertical profile of the estimated maximum run-up elevation h_{max} for any parcel of the fluid at initial height z, with the maximum run-up height H_{max} for the overall flow indicated as a red square. (H) Distribution of the H_{max}/h for the experimental density currents at 3 m downstream from the channel mouth along the channel-basin centreline for the first 35 s time window after the current head in the unconfined reference experiment.

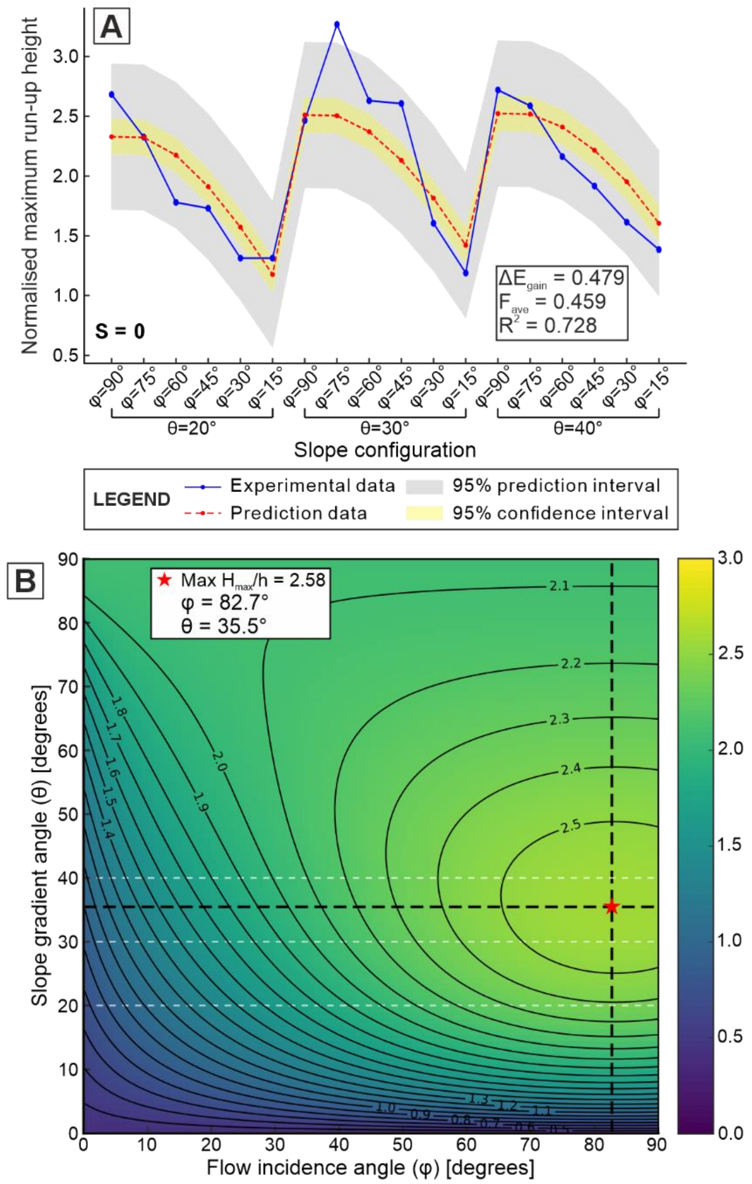

Fig. S3. (A) Comparison between observed and predicted values of normalised maximum run-up height upslope for our 18 ramp experiments. The results of optimised ΔE_{gain} and F_{ave} using Equation S5 best-fit for the observed experimental data points and the fit accuracy (R^2) are reported in the bottom right box. The input quantities in the model are set to constant, representative for the current physical experiments in the first 5 s after the current head (z = 0.045 m, ρ_z = 999.8 kg/m^3, $\Delta\rho_z$ = 0.22 kg/m^3, h = 0.11 m, u_z= 0.0243 m/s, v_z = -0.12u_z, w_z = 0.09u_z). (B) Contour map of modelled normalised maximum run-up height, H_{max}/h, as a function of the flow incidence angle onto the slope (φ) and slope gradient (θ), with the input variables set to constant values typical of current physical experiments and the optimised

ΔE_{gain} and F_{ave}. A critical θ and φ for the current setting is shown to exist, whereby H_{max}/h reaches its maximum value.

SUPPLEMENTARY VIDEO CAPTIONS

Movie S1. Annotated video illustrating the behaviour of density currents upon incidence with an oblique topographic slope (Experiment S40°IN75°).